Monthly Notices
of the
ROYAL ASTRONOMICAL SOCIETY

MNRAS **458,** 4321–4344 (2016)
Advance Access publication 2016 March 10

doi:10.1093/mnras/stw564

The SCUBA-2 Cosmology Legacy Survey: galaxies in the deep 850 μm survey, and the star-forming 'main sequence'

M. P. Koprowski,[1⋆] J. S. Dunlop,[1⋆] M. J. Michałowski,[1] I. Roseboom,[1] J. E. Geach,[2] M. Cirasuolo,[1,3] I. Aretxaga,[4] R. A. A. Bowler,[1] M. Banerji,[5] N. Bourne,[1] K. E. K. Coppin,[2] S. Chapman,[6] D. H. Hughes,[4] T. Jenness,[7] R. J. McLure,[1] M. Symeonidis[8] and P. van der Werf[9]

[1]*SUPA, Institute for Astronomy, University of Edinburgh, Royal Observatory, Edinburgh EH9 3HJ, UK*
[2]*Centre for Astrophysics Research, Science & Technology Research Institute, University of Hertfordshire, College Lane, Hatfield AL10 9AB, UK*
[3]*UK Astronomy Technology Centre, Royal Observatory, Edinburgh EH9 3HJ, UK*
[4]*Instituto Nacional de Astrofisica, Optica y Electronica (INAOE), Aptdo. Postal 51 y 216, 72000 Puebla, Pue., Mexico*
[5]*Institute of Astronomy, University of Cambridge, Madingley Road, Cambridge CB3 0HA, UK*
[6]*Department of Physics and Atmospheric Science, Dalhousie University, Coburg Road, Halifax, NS B3H 1A6, Canada*
[7]*LSST Project Office, 933 N. Cherry Ave, Tucson, AZ 85719 USA*
[8]*Mullard Space Science Laboratory, University College London, Holmbury St. Mary, Dorking, Surrey RH5 6NT, UK*
[9]*Leiden Observatory, Leiden University, PO Box 9513, NL-2300 RA Leiden, the Netherlands*

Accepted 2016 March 7. Received 2016 March 6; in original form 2015 September 21

ABSTRACT

We investigate the properties of the galaxies selected from the deepest 850-μm survey undertaken to date with (Submillimetre Common-User Bolometer Array 2) SCUBA-2 on the James Clerk Maxwell Telescope as part of the SCUBA-2 Cosmology Legacy Survey. A total of 106 sources ($>5\sigma$) were uncovered at 850 μm from an area of $\simeq$150 arcmin^2 in the centre of the COSMOS/UltraVISTA/Cosmic Assembly Near-infrared Deep Extragalactic Legacy Survey (CANDELS) field, imaged to a typical depth of $\sigma_{850} \simeq 0.25$ mJy. We utilize the available multifrequency data to identify galaxy counterparts for 80 of these sources (75 per cent), and to establish the complete redshift distribution for this sample, yielding $\bar{z} = 2.38 \pm 0.09$. We have also been able to determine the stellar masses of the majority of the galaxy identifications, enabling us to explore their location on the star formation rate:stellar mass (SFR:M^*) plane. Crucially, our new deep 850-μm-selected sample reaches flux densities equivalent to SFR $\simeq$ 100 $M_\odot$ yr^{-1}, enabling us to confirm that sub-mm galaxies form the high-mass end of the 'main sequence' (MS) of star-forming galaxies at $z > 1.5$ (with a mean specific SFR of sSFR $= 2.25 \pm 0.19$ Gyr^{-1} at $z \simeq 2.5$). Our results are consistent with no significant flattening of the MS towards high masses at these redshifts. However, our results add to the growing evidence that average sSFR rises only slowly at high redshift, resulting in $\log_{10}$sSFR being an apparently simple linear function of the age of the Universe.

Key words: galaxies: evolution – galaxies: high-redshift – galaxies: starburst – cosmology: observations – submillimetre: galaxies.

1 INTRODUCTION

It is now well known that approximately half of the starlight in the Universe is re-processed by cosmic dust and re-emitted at far-infrared wavelengths (Dole et al. 2006). However, due to a combination of the inescapable physics of diffraction, the molecular content of our atmosphere, and the technical difficulties of sensitive high-background imaging, it has proved difficult to connect the UV/optical and far-infrared/sub-mm views of the Universe into a consistent and complete picture of galaxy formation/evolution. Thus, while the advent of Submillimetre Common-User Bolometer Array (SCUBA) on the 15-m James Clerk Maxwell Telescope (JCMT) in the late 1990s (Holland et al. 1999) enabled the first discovery of distant dusty galaxies with star formation rates SFR $\simeq$ 1000 $M_\odot$ yr^{-1} (e.g. Smail, Ivison & Blain 1997; Barger et al. 1998; Hughes et al. 1998; Eales et al. 1999), such objects initially seemed too extreme and unusual to be easily related to the more

⋆ E-mail: mpk@roe.ac.uk (MPK); jsd@roe.ac.uk (JSD)
† Scottish Universities Physics Alliance

© 2016 The Authors
Published by Oxford University Press on behalf of the Royal Astronomical Society

numerous, 'normal' star-forming galaxies being uncovered at UV/optical wavelengths at comparable redshifts ($z \simeq 2$–4) by Keck (e.g. Steidel et al. 1996) and the *Hubble Space Telescope* (HST; e.g. Madau et al. 1996). In recent years, the study of rest-frame UV-selected galaxies has been extended out beyond $z \simeq 10$ (see Dunlop 2013 for a review, and Coe et al. 2013; Ellis et al. 2013; McLure et al. 2013; Bowler et al. 2012, 2014; Oesch et al. 2014; Bouwens et al. 2015; Finkelstein et al. 2015; Ishigaki et al. 2015; McLeod et al. 2015), while a number of sub-mm-selected galaxies have now been confirmed at $z > 4$ (Capak et al. 2008; Coppin et al. 2009; Daddi et al. 2009a,b; Knudsen et al. 2010; Riechers et al. 2010; Cox et al. 2011; Combes et al. 2012; Weiss et al. 2013) with the current redshift record holder at $z = 6.34$ (Riechers 2013). However, while such progress is exciting, at present there is still relatively little meaningful intersection between these UV/optical and far-infrared/sub-mm studies of the high-redshift Universe (although see Walter et al. 2012).

At more moderate redshifts, however, recent years have seen increasingly successful efforts to bridge the gap between the unobscured and dust-enshrouded views of the evolving galaxy population. Of particular importance in this endeavour has been the power of deep 24 μm imaging with the MIPS instrument on board *Spitzer*, which has proved capable of providing a useful estimate of the dust-obscured star formation activity in a significant fraction of optically selected galaxies out to $z \simeq 1.5$–2 (e.g. Caputi et al. 2006; Elbaz et al. 2010). Indeed, MIPS imaging of the GOODS survey fields played a key role in establishing what has proved to be a fruitful framework for the study of galaxy evolution, namely the existence of a so-called main sequence (MS) for star-forming galaxies, in which star formation rate is found to be roughly proportional to stellar mass (SFR $\propto M_*$; Daddi et al. 2007; Noeske et al. 2007; Renzini & Peng 2015), with a normalization that rises with increasing redshift (e.g. Santini et al. 2009; Oliver et al. 2010; Elbaz et al. 2011; Karim et al. 2011; Rodighiero et al. 2011, 2014; Johnston et al. 2015; Salmon et al. 2015; Schreiber et al. 2015; Tasca et al. 2015).

Interest in the MS of star-forming galaxies has continued to grow (see Speagle et al. 2014 for a useful and comprehensive overview), not least because of the difficulty encountered by most current models of galaxy formation in reproducing its apparently rapid evolution between $z \simeq 0$ and $z \simeq 2$ (e.g. Mitchell et al. 2014). However, it has, until now, proved very difficult to extend the robust study of the MS beyond $z \simeq 2$ and to the highest masses (e.g. Steinhardt et al. 2014; Leja et al. 2015; Salmon et al. 2015). This is because an increasing fraction of star formation is enshrouded in dust in high-mass galaxies, and *Spitzer* MIPS and *Herschel* become increasingly ineffective in the study of dust-enshrouded SF with increasing redshift (due to a mix of wavelength and resolution limitations), as the far-infrared emission from dust is redshifted into the sub-mm/mm regime.

A complete picture of star formation in more massive galaxies at high redshift can therefore only be achieved with ground-based sub-mm/mm observations, which provide image quality at sub-mm wavelengths that is vastly superior to what can currently be achieved from space. The challenge, then, is to connect the population of dusty, rapidly star-forming high-redshift galaxies revealed by ground-based sub-mm/mm surveys to the population of more moderate star-forming galaxies now being revealed by optical/near-infrared observations out to the highest redshifts. On a source-by-source basis, this can now be achieved by targeted follow-up of known optical/infrared-selected galaxies with ALMA (e.g. Ono et al. 2014). However, this will inevitably produce a biased perspective which can only be re-balanced by also continuing to undertake ever deeper and wider sub-mm/mm surveys capable of detecting highly obscured objects (again, potentially, for ALMA follow-up; Hodge et al. 2013; Karim et al. 2013), and thus completing our census of star-forming galaxies in the young Universe.

This is one of the primary science drivers for the SCUBA-2 Cosmology Legacy Survey (S2CLS). The S2CLS is advancing the field in two directions. First, building on previous efforts with SCUBA (e.g. Scott et al. 2002; Coppin et al. 2006; Scott, Dunlop & Serjeant 2006), MAMBO (e.g. Bertoldi et al. 2000; Greve et al. 2004), LABOCA (e.g. Weiss et al. 2009) and AzTEC (e.g. Austermann et al. 2010; Scott et al. 2012), the S2CLS is using the improved mapping capabilities of SCUBA-2 (Holland et al. 2013) to extend surveys for bright ($S_{850} > 5$ mJy) sub-mm sources to areas of several square degrees, yielding large statistical samples of such sources (>1000). Secondly, the S2CLS is exploiting the very dryest (Grade-1) conditions at the JCMT on Mauna Kea, Hawaii, to obtain very deep 450 μm imaging of small areas of sky centred on the *HST* CANDELS fields (Grogin et al. 2011), which provide the very best multiwavelength supporting data to facilitate galaxy counterpart identification and study. The first such deep 450 μm image has been completed in the centre of the COSMOS-CANDELS/UltraVISTA field, with the results reported by Geach et al. (2013) and Roseboom et al. (2013). Here, we utilize the ultradeep 850 μm image of the same region, which was automatically obtained in parallel with the 450 μm imaging. While the dryest weather is more essential for the shorter wavelength imaging at the JCMT, such excellent conditions (and long integrations) inevitably also benefit the parallel 850 μm imaging. Consequently, the 850 μm data studied here constitute the deepest ever 850 μm survey ever undertaken over an area $\simeq$150 arcmin^2.

The depth of the new S2CLS 850 μm imaging is typically $\sigma_{850} \simeq 0.25$ mJy. This is important because it means that galaxies detected near the limit of this survey have SFR $\simeq 100\,\mathrm{M}_\odot\,\mathrm{yr}^{-1}$, which is much more comparable to the highest SFR values derived from UV/optical/near-infrared studies than the typical SFR sensitivity achieved with previous single-dish sub-mm/mm imaging (i.e. SFR $\simeq 1000\,\mathrm{M}_\odot\,\mathrm{yr}^{-1}$ as a result of $\sigma_{850} \simeq 2$ mJy). Ultimately, of course, ALMA will provide even deeper sub-mm surveys with the resolution required to overcome the confusion limit of the single-dish surveys. However, because of its modest field of view (∼20 arcsec at 850 μm), it is observationally expensive to survey large areas of blank sky with ALMA, and contiguous mosaic surveys are hard to justify at depths where the source surface density is significantly less than one per pointing. Thus, at the intermediate depths probed here, the S2CLS continues to occupy a unique and powerful niche in the search for dust-enshrouded star-forming galaxies.

The fact that previous sub-mm/mm surveys were only generally capable of detecting very extreme objects has undoubtedly contributed to some of the confusion/controversy over the nature of galaxies selected at sub-mm/mm wavelengths; while Michałowski et al. (2012b) and Roseboom et al. (2013) have presented evidence that sub-mm selected galaxies lie on the high-mass end of the MS at $z = 2$–3, others have continued to argue that, like many local ULIRGs, they are extreme pathological objects driven by recent major mergers (e.g. Hainline et al. 2011). Some of this debate reflects disagreements over the stellar masses of the objects rather than their star formation rates (e.g. Michałowski et al. 2014). Nevertheless, the fact that even high-mass galaxies on the MS lay right at the detection limits of previous sub-mm surveys inevitably resulted in many sub-mm-selected objects apparently lying above the MS, fuelling arguments about whether they were indeed significant

outliers, or whether we have simply been uncovering the positive tail in SFR around the MS (see Roseboom et al. 2013).

The much deeper 850 μm survey studied here is capable of settling this issue, provided of course we can overcome the now customary challenge of identifying the galaxy counterparts of most of the sub-mm sources, and determining their redshifts, SFRs and stellar masses (M_*) (e.g. Ivison et al. 2007; Dunlop et al. 2010; Biggs et al. 2011; Wardlow et al. 2011; Michałowski et al. 2012a; Koprowski et al. 2014). However, in this effort, we are also aided by the depth of the SCUBA-2 data, and by the additional positional information provided by the (unusual) availability of 450 μm detections (with FWHM $\simeq$ 8 arcsec) for 50 per cent of the sample. We also benefit hugely from the unparalleled multifrequency supporting data available in the CANDELS fields, provided by *HST*, Subaru, Canada–France–Hawaii Telescope (CFHT), Vista, *Spitzer*, *Herschel* and the Very Large Array (VLA).

This paper is structured as follows. In Section 2, we present the SCUBA-2 and other multiwavelength data utilized in this work. Then, in Section 3, we explain how optical/infrared galaxy counterparts were established for the SCUBA-2 sources, and summarize the resulting identification statistics. Next, in Section 4, we explain the calculation of the photometric redshifts, both from the optical–infrared data for the galaxy identifications, and from the long-wavelength data for the unidentified or spuriously identified sources. The resulting redshift distribution for the complete 106-source S2CLS sample is presented here, and compared with the redshift distributions derived from other recent sub-mm/mm surveys. In Section 5, we move on to derive and discuss the physical properties of the sources (such as dust temperature, bolometric luminosity, SFR, stellar mass), culminating in the calculation of specific SFR and the exploration of the star-forming MS. Our conclusions are summarized in Section 6. All magnitudes are quoted in the AB system (Oke 1974; Oke & Gunn 1983) and all cosmological calculations assume $\Omega_{\rm M} = 0.3$, $\Omega_\Lambda = 0.7$ and $H_0 = 70$ km s^{-1} Mpc^{-1}.

2 DATA

2.1 SCUBA-2 imaging and source extraction

We used the deep 850 μm and 450 μm S2CLS imaging of the central $\simeq$ 150 arcmin^2 of the COSMOS/UltraVISTA field, coincident with the *Spitzer* SEDS (Ashby et al. 2013) and *HST* CANDELS (Grogin et al. 2011) imaging. The observations were taken with SCUBA-2 mounted on the JCMT between October 2011 and March 2013, reaching depths of $\sigma_{850} \simeq 0.25$ mJy and $\sigma_{450} \simeq 1.5$ mJy (Geach et al. 2013, Roseboom et al. 2013, Geach et al., in preparation). In order to enable effective 450 μm observations, only the very best/dryest conditions were used (i.e. $\tau_{225\,\rm GHz} < 0.05$), and to maximize depth the imaging was undertaken with a 'daisy' mapping pattern (Bintley et al. 2014).

The details of the reduction process are described in Roseboom et al. (2013), and so only a brief description is given here.

The data were reduced with the SMURF package[1] V1.4.0 (Chapin et al. 2013) with flux calibration factors (FCFs) of 606 Jy pW^{-1} Beam^{-1} for 450 μm and 556 Jy pW^{-1} Beam^{-1} for 850 μm (Dempsey et al. 2013).

The noise-only maps were constructed by inverting an odd half of the ∼30 min scans and stacking them all together. In the science maps, the large-scale background was removed by applying a high-pass filter above 1.3 Hz to the data (equivalent to 120 arcsec given the SCUBA-2 scan rate). Then a 'whitening filter' was applied to suppress the noise in the map whereby the Fourier transform of the map is divided by the noise-only map power spectrum, normalized by the white-noise level and transformed back into real space. The effective point-source response function (PRF) was constructed from a Gaussian with a full width at half-maximum (FWHM) of 14.6 arcsec following the same procedure. Finally, the real sources with a signal-to-noise ratio (SNR) of better than 5 were extracted by convolving the whitened map with the above PRF (see section 4.2 of Chapin et al. 2013).

The 850 μm image and the sources extracted from it are shown in Fig. 1, while the positions and sub-mm photometry for the sources are listed in Appendix, Table A1.

A total of 106 850 μm sources were found within the map with an SNR >5. The photometry at 450 μm was performed in the same manner, but assuming the PRF at 450 μm to be a Gaussian of FWHM = 8 arcsec. The 450 μm counterparts to the 850 μm sources were adopted if a 450 μm-selected source was found within 6 arcsec of the 850 μm centroid. As seen in Fig. 2, 53 850 μm sources have 450 μm counterparts with the mean separation of 2.7 ± 0.2 arcsec. Otherwise, for the purpose of Spectral Energy Distribution (SED) fitting, the 450 μm flux density was measured at the 850 μm position (flags 1 and 0 in Table A1, respectively).

The completeness of the 850 μm catalogue was assessed by injecting sources of known flux density into the noise-only maps. Overall 10^4 objects were used, split into 10 logarithmically spaced flux-density bins between 1 and 60 mJy. In total 2000 simulated maps were created, and the source extraction was performed in the same way as with the real maps. The completeness was then assessed by dividing the number of extracted sources by the number of sources inserted into the noise-only maps, and the results are shown in Fig. 3.

2.2 Supporting multifrequency data

This first deep S2CLS pointing within the COSMOS/UltraVISTA field was chosen to maximize the power of the available ancillary multiwavelength data, in particular the *HST* Cosmic Assembly Near-infrared Deep Extragalactic Legacy Survey (CANDELS)[2] imaging (Grogin et al. 2011). In addition, the optical Canada–France–Hawaii Telescope Legacy Survey (CFHTLS; Gwyn 2012), the Subaru/Suprime-Cam z'-band (Taniguchi et al. 2007; Furusawa et al., in preparation) and UltraVISTA near-infrared data (McCracken et al. 2012) were used. The catalogues were made by smoothing all the ground-based and *HST* data to the seeing of the UltraVISTA *Y*-band image with the Gaussian of FWHM = 0.82 arcsec (for details, see Bowler et al. 2012, 2014, 2015). The catalogue was selected in the smoothed CANDELS *H*-band image and photometry was measured in 3 arcsec apertures using the dual-mode function in SExtractor (Bertin & Arnouts 1996) on all other PSF homogenized images.

The *Spitzer* IRAC flux densities at 3.6 μm and 4.5 μm were measured from the S-COSMOS survey (Sanders et al. 2007), after image deconfusion based on the UltraVISTA K_s-band image; using GALFIT (Peng et al. 2002) the K_s-band images were modelled, and the corresponding structural parameters were then applied to both the 3.6 μm and 4.5 μm data and the flux-densities allowed to vary until

[1] http://www.starlink.ac.uk/docs/sun258.htx/sun258.html

[2] http://candels.ucolick.org

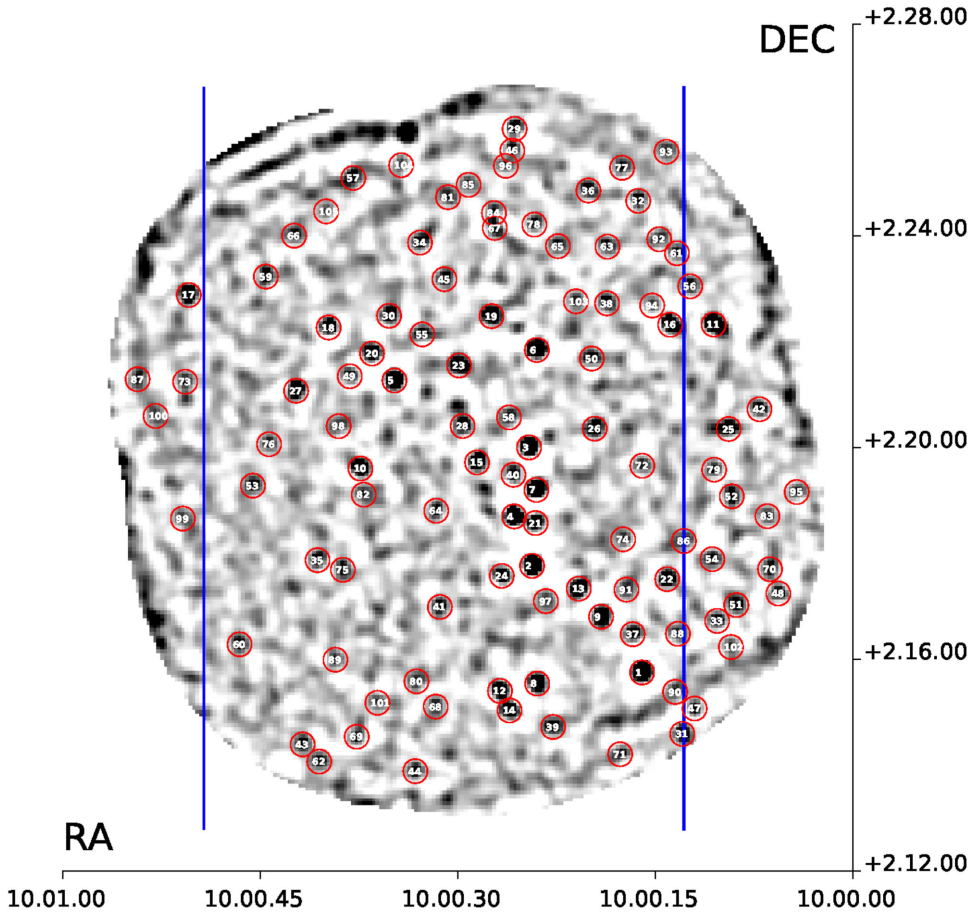

Figure 1. The SCUBA-2 850 μm map of the central sub-region of the COSMOS/UltraVISTA field. All 106 sources extracted with SNR $> 5\sigma$ are highlighted with red circles, and marked with the ID number by which the sources are tabulated in Table A1. As explained in Section 2.2 two optical–infrared catalogues were utilized in this work. The catalogue with the *HST* CANDELS and deconfused IRAC SEDS data, which contains sources extracted from the map covering the CANDELS area (enclosed by the two blue vertical lines), and the catalogue without the *HST* data (outside the blue lines) which was used only for 20 sources.

the optimum fit to the IRAC image of each object was achieved (after convolution with the appropriate PSFs). The infinite-resolution scaled model IRAC images created in this way were then smoothed again to match the seeing of the UltraVISTA *Y*-band image, after which the IRAC flux densities were measured within 3 arcsec apertures. For the small number of objects selected from the SCUBA-2 map which lay outside the area with CANDELS *HST* imaging (see Fig. 1), the K_s-band UltraVISTA image was used as the primary image for near-infrared candidate counterpart selection.

The 24 μm catalogue was constructed using the MIPS 24 μm imaging from the S-COSMOS survey (Le Floc'h et al. 2009). The source extraction was performed on the publicly available imaging using the STARFINDER IDL package (Diolaiti et al. 2000). The resulting catalogue covers ∼2.1 deg^2 and reaches the depth of $\sigma \simeq 13$ μJy (for details, see Roseboom et al. 2013).

For the extraction of far-infrared flux densities and limits we used the *Herschel* (Pilbratt et al. 2010) Multi-tiered Extragalactic Survey (Oliver et al. 2012) and the Photodetector Array Camera and Spectrometer (PACS; Poglitsch et al. 2010) Evolutionary Probe (Lutz et al. 2011) data obtained with the Spectral and Photometric Imaging Receiver (SPIRE; Griffin et al. 2010) and PACS instruments, covering the entire COSMOS field. We utilized *Herschel* maps at 100, 160, 250, 350 and 500 μm with beam sizes of 7.39, 11.29, 18.2, 24.9 and 36.3 arcsec, and 5σ sensitivities of 7.7, 14.7, 24.0, 27.5 and 30.5 mJy, respectively. We obtained the fluxes of each SCUBA-2 source in the following way. We extracted 120-arcsec-wide stamps from each *Herschel* map around each SCUBA-2 source and used the PACS (100, 160 μm) maps to simultaneously fit Gaussians with the FWHM of the respective map, centred at all radio and 24 μm sources located within these cut-outs, and at the positions of the SCUBA-2 optical identifications (IDs, or just sub-mm positions if no IDs were selected). Then, to deconfuse the SPIRE (250, 350 and 500 μm) maps in a similar way, we used the positions of the 24 μm sources detected with PACS (at $>3\sigma$), the positions of all radio sources, and the SCUBA-2 ID positions.

Finally, the VLA COSMOS Deep catalogue was used where the additional VLA A-array observations at 1.4 GHz were obtained and combined with the existing data from the VLA-COSMOS Large project (for details, see Schinerrer et al. 2010). This catalogue covers $\simeq 250$ arcmin^2 and reaches a sensitivity of $\sigma = 12$ μJy beam^{-1}.

3 SCUBA-2 SOURCE IDENTIFICATIONS

In order to find the optical counterparts for sub-mm sources, for which positions are measured with relatively large beams, a simple closest-match approach is not sufficiently accurate. We therefore use the method outlined in Dunlop et al. (1989) and Ivison et al. (2007) where we adopt the 2.5σ search radius around the SCUBA-2

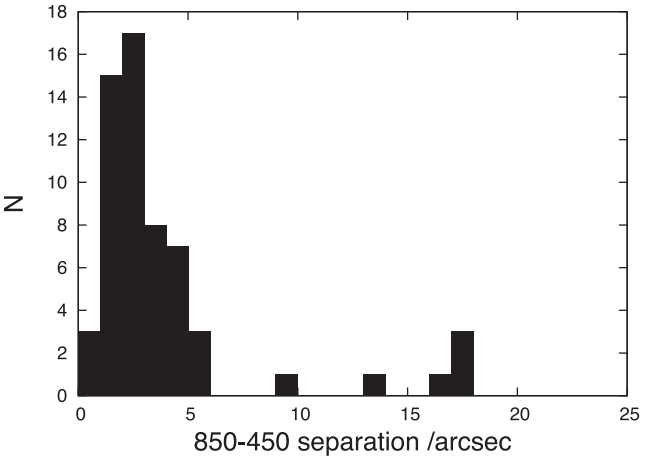

Figure 2. The distribution of the separation between 850 μm and 450 μm positions, where the maximum search radius was set to 25 arcsec. Based on this distribution, it was decided that a 450 μm source and an 850 μm source lying within 6 arcsec of each other correspond to the same galaxy (for such pairs, the mean separation is 2.7 ± 0.2 arcsec). As detailed in Table A1, there are 53 850 μm sources with 450 μm counterparts (50 per cent).

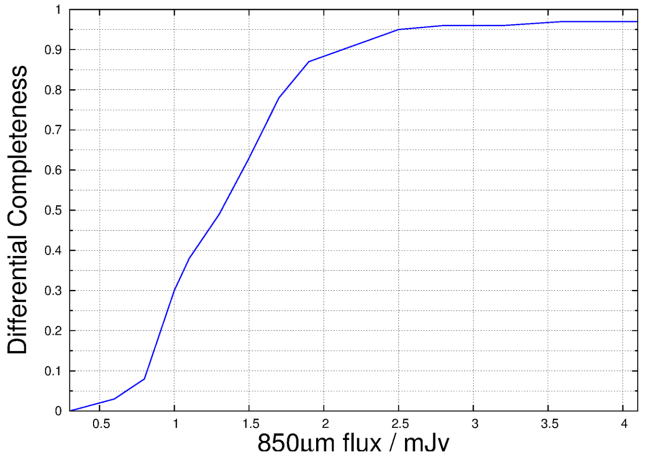

Figure 3. Completeness of the 850 μm source sample as a function of flux density based on 2000 simulated maps with source extraction performed on 10^4 artificially created objects.

position based on the SNR: $r_s = 2.5 \times 0.6 \times \mathrm{FWHM/SNR}$, where FWHM $\simeq$ 15 arcsec. In order to account for systematic astrometry shifts (caused by pointing inaccuracies and/or source blending; e.g. Dunlop et al. 2010), we enforce a minimum search radius of 4.5 arcsec. Within this radius we calculate the corrected Poisson probability, p, that a given counterpart could have been selected by chance.

For reasons explained below, the VLA 1.4 GHz and *Spitzer* MIPS 24 μm and IRAC 8 μm (with addition of 3.6 μm) bands were chosen for searching for galaxy counterparts. In the case of the MIPS 24 μm band, the minimum search radius was increased to 5 arcsec to account for the significant MIPS beam size ($\simeq$ 6 arcsec). The optical/near-infrared catalogues were then matched with these coordinates using a search radius of $r = 1.5$ arcsec and the closest match taken to be the optical counterpart. In addition, we utilized the *Herschel*, SCUBA-2 and VLA photometry to help isolate likely incorrect identifications (Section 4.2).

The results of the identification process are summarized in Table A2, where the most reliable IDs ($p \leq 0.05$) are marked in bold,

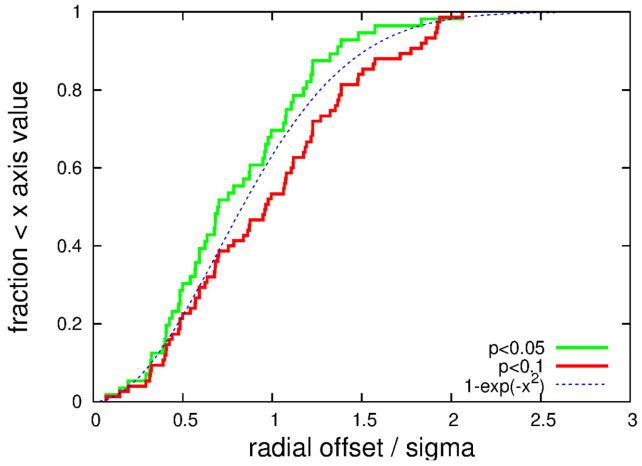

Figure 4. A demonstration that the distribution of positional offsets between the 850 μm sources and identified galaxy counterparts is consistent with statistical expectations. The histograms show the cumulative distribution of positional offset divided by positional uncertainty, where the positional uncertainty for each SCUBA-2–counterpart association is derived by calculating the uncertainty in the position of both the 850 μm source and its counterpart (based on the standard formula $\sigma = 0.6 \times \mathrm{FWHM/SNR}$; see Section 3), and adding these in quadrature, with an additional 2 arcsec added in quadrature to account for JCMT pointing uncertainties. The histograms show the distributions for the most secure $p < 0.05$, and less secure $p < 0.1$ identifications, while the curve shows the prediction assuming a Gaussian distribution. This plot provides reassurance that, at the flux level of the sources considered here, source confusion has not significantly distorted the source positions, and source blending is not a significant issue.

the tentative IDs ($0.05 < p \leq 0.1$) are marked in italics, and incorrectly identified sources (as discussed in Section 4.2) are marked with asterisks.

Given the depth of the 850 μm imaging utilized here, it is important to check that source positions have not been significantly distorted by source confusion. We have therefore checked that the distribution of positional offsets between the 850 μm sources and their adopted multifrequency counterparts is as expected, assuming the standard formula for positional uncertainty (i.e. $\sigma = 0.6 \times$ FWHM/SNR). The results, shown in Fig. 4, provide reassurance that the vast majority of source positions have not been significantly distorted by confusion/blending, and that our association process is statistically valid.

3.1 Radio and 24 μm counterparts

The 850 μm band is sensitive to the cool dust re-radiating energy absorbed from hot, young stars. The radio band also traces recent star formation via synchrotron radiation from relativistic electrons produced within supernovae (SNe; Condon 1992). The 24 μm waveband is in turn sensitive to the emission from warm dust, and since sub-mm-selected galaxies are dusty star-forming galaxies, they are also expected to be reasonably luminous in this band. There is thus a good physical motivation for searching for the counterparts of SCUBA-2 sources in the VLA and MIPS imaging. In addition, the surface density of sources in these wavebands is low enough for chance positional coincidences to be rare (given a sufficiently small search radius).

As seen in Table 1 (before the corrections of Section 4.2), at 1.4 GHz the ID success rate is only 14 per cent (15 out of 106 sources, all with $p \leq 0.05$) but at 24 μm the success rate is 69 per cent

Table 1. The radio/infrared/optical identification statistics for the 850 μm S2CLS COSMOS sample used in this work. The number of reliably (with a probability of chance association, $p < 0.05$), tentatively (with $0.05 < p \leq 0.1$) and all ($p \leq 0.1$) identified sources are given (with the percentage, out of 106 sources, in brackets). The columns give the ID success rate at a given band followed by the overall radio/mid-infrared ID success rate, the raw optical ID success rate and revised optical ID success rate after checking for consistency with the long-wavelength photometric redshifts (see Fig. 5 and Section 4.2).

	1.4 GHz	24 μm	8 μm	Radio/IR overall	Optical before corr.	optical After corr.
Reliable ($p \leq 0.05$)	15 (14 per cent)	62 (58 per cent)	37 (35 per cent)	67 (63 per cent)	67 (63 per cent)	54 (51 per cent)
Tentative ($0.05 < p \leq 0.1$)	0 (0 per cent)	11 (10 per cent)	20 (19 per cent)	13 (12 per cent)	13 (12 per cent)	8 (8 per cent)
All ($p \leq 0.1$)	15 (14 per cent)	73 (69 per cent)	57 (54 per cent)	80 (75 per cent)	80 (75 per cent)	62 (58 per cent)

(73 out of 106, 62 of which have $p \leq 0.05$). Combining both methods, the successful identification rate is 70 per cent (74 out of 106, 63 of which have $p \leq 0.05$). The striking difference in these statistics is due to the fact that the S-COSMOS 24 μm imaging utilized here is relatively deeper than the radio data currently available in the COSMOS field.

3.2 8 μm counterparts

In order to maximize the identification success rate, we also searched for counterparts in the S-COSMOS IRAC 8 μm imaging. At the redshifts of interest, this waveband traces the rest-frame near-infrared light coming from the older, mass-dominant stellar populations in galaxies. Given the growing evidence that sub-mm galaxies are massive, it is expected that they will be more luminous than average in this waveband (e.g. Dye et al. 2008; Michałowski, Hjorth & Watson 2010; Biggs et al. 2011; Wardlow et al. 2011). We found that 57 of the 106 SCUBA-2 sources (54 per cent) had 8 μm counterparts, 37 of which have $p \leq 0.05$. However, unsurprisingly, several of these identifications simply confirmed the identifications already secured via the radio and/or 24 μm cross-matching, and the search for 8 μm counterparts only added five new identifications (two of which have $p \leq 0.05$) to the results described in the previous subsection.

3.3 Optical counterparts

In total, therefore, we identified radio/mid-infrared counterparts for 80 of the 106 SCUBA-2 850 μm sources (67 of which have $p \leq 0.05$; see Table A2), and hence achieved an identification success rate of 75 per cent. The identification success rate achieved in each individual waveband is given in Table 1. In addition, we present postage-stamp images for all the sources in the online version (Fig. B1), with all the identifications marked with the appropriate symbols.

To complete the connection between the SCUBA-2 sources and their host galaxies, within the area covered by the CANDELS *HST* WFC3/IR imaging (Fig. 1) we matched the statistically significant mid-infrared and radio counterparts to the galaxies in the CANDELS H_{160}-band imaging using a maximum matching radius of 1.5 arcsec. This yielded accurate positions for the optical identifications of 60 of the SCUBA-2 sources (Table A3). For those few SCUBA-2 sources which lie outside the CANDELS *HST* imaging, we matched the statistically significant mid-infrared and radio counterparts to the galaxies in the K_s-band UltraVISTA imaging (using the same maximum matching radius). This yielded accurate positions for the optical identifications of the remaining 20 sources (Table A4). We note that galaxies SC850-37, 46 and 61, even though successfully identified in the optical/near-infrared, turned out to be too close to a foreground star for reliable photometry (Fig. B1 in the online version) and therefore no optical redshifts or stellar masses were derived and utilized in the subsequent analysis.

4 REDSHIFTS

4.1 Photometric redshifts

For all the identified sources, the multiband photometry given in Tables A3 and A4 was used to derive optical–infrared photometric redshifts using a χ^2-minimization method (Cirasuolo et al. 2007, 2010) with a template-fitting code based on the HYPERZ package (Bolzonella, Miralles & Pelló 2000). To create template galaxy SEDs, the stellar population synthesis models of Bruzual & Charlot (2003) were applied, using the Chabrier (2003) stellar initial mass function (IMF) with a lower and upper mass cut-off of 0.1 and 100 $M_\odot$, respectively. A range of single-component star formation histories were explored, as well as double-burst models. Metallicity was fixed at solar, but dust reddening was allowed to vary over the range $0 \leq A_V \leq 6$, assuming the law of Calzetti et al. (2000). The HI absorption along the line of sight was applied according to Madau (1995). The optical–infrared photometric redshifts for the 77 optically identified sources for which photometry could be reliably extracted (i.e. the 80 identified sources excluding SC850-37, 46 and 61) are given in Table A5. Also given in this table are the optical spectroscopic redshifts where available. We note that, in general, $z_{\rm spec}$ and $z_{\rm p}$ are in excellent agreement, except for the two SCUBA-2 sources which are associated with active galactic nuclei (AGN; sources 65 and 72), presumably because no AGN template was included in the photometric redshift fitting procedure.

In addition, for *every* SCUBA-2 source we used the 450 and 850 μm photometry as well as the *Herschel* 100, 160, 250, 350, 500 μm and VLA 1.4 GHz flux densities (or limits) to obtain 'long-wavelength' photometric redshifts ($z_{\rm LW}$). This was achieved by fitting the average SED template of sub-mm galaxies from Michałowski et al. (2010) to the measured flux densities and errors in all eight of these long-wavelength bands (including flux-density measurements corresponding to nondetections). The resulting 'long-wavelength' redshift estimates for all 106 sources are also given in Table A5.

4.2 Redshift/identification refinement

Given the statistical nature of the identification process described above, there is always a possibility that some identifications are incorrect (as revealed by interferometric follow-up – e.g. Hodge et al. 2013; Koprowski et al. 2014), and indeed, even when the probability of chance coincidence is extremely small, it can transpire that the optical counterpart is not, in fact, the correct galaxy identification,

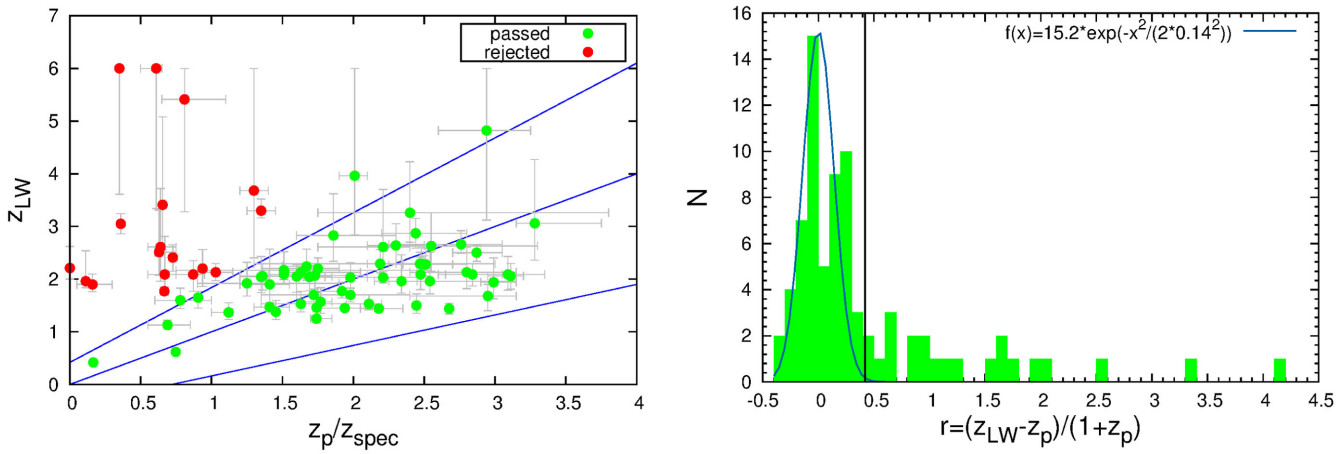

Figure 5. The left-hand panel shows the 'long-wavelength' photometric redshifts (z_{LW}) derived for the SCUBA-2 sources plotted against the optical–infrared photometric redshifts (z_p) of the optical identifications (see Section 4.2). The central blue solid line shows the 1:1 relation. As illustrated in the right-hand panel, the sources lying below the 1:1 relation display a distribution of normalized redshift offsets (i.e. $r = (z_{LW} - z_p)/(1 + z_p)$) which is approximately Gaussian with $\sigma = 0.14$. The positive side of this distribution is also reasonably well fitted by this same Gaussian, but there is a long positive tail, indicative of the fact that a significant subset of the identifications have a value of z_p which is much smaller than the (identification independent) 'long-wavelength' photometric redshift of the SCUBA-2 source (z_{LW}). Given the potential for misidentification (e.g. through galaxy–galaxy gravitational lensing), we view such discrepancies as evidence that z_p, or more likely the galaxy identification itself, is in error. The upper and lower blue solid lines in the left-hand panel show the $\pm 3\sigma$ limits of the Gaussian distribution, and so we choose to reject the optical identifications (and hence also z_p) for the sources that lie above the 3σ limit (red dots). This same 3σ limit is shown by the black vertical line in the right-hand panel.

but is actually an intervening galaxy, gravitationally lensing a more distant sub-mm source (e.g. Dunlop et al. 2004). In either case, a misidentification will lead to an underestimation of the true redshift of the sub-mm source, and indeed dramatic discrepancies between z_p and z_{LW} can potentially be used to isolate misidentified sources.

In Fig. 5, we have therefore plotted z_{LW} versus z_p in an attempt to test the consistency of these two independent redshift estimators. From this plot, it can be seen that, for the majority of sources, the two redshift estimates are indeed consistent, with the normalized offset in z_{LW} ($r = (z_{LW} - z_p)/(1 + z_p)$) displaying a Gaussian distribution with $\sigma = 0.14$. However, there is an extended *positive* tail to this distribution, indicative of the fact that a significant subset of the identifications have a value of z_p which is much smaller than the (identification independent) 'long-wavelength' photometric redshift of the SCUBA-2 source, z_{LW}. Given the aforementioned potential for misidentification (and concomitant redshift underestimation), we have chosen to reject the optical identifications (and hence also z_p) for the sources that lie more than 3σ above the 1:1 redshift relation (see Fig. 5 and caption for details). This may lead to the rejection of a few correct identifications, but this is less important than the key aim of removing any significant redshift biases due to misidentifications, and also the value of retaining only the most reliable set of identified sources for further study.

The effect of this cut is the rejection of 18 of the 80 optical identifications derived in Section 3. These rejected optical IDs are flagged with asterisks in Table A2 and zeros in Table A5. We emphasize that the rejection of these low-redshift identifications does not impact significantly on the investigation of the physical properties of the sub-mm sources at $z \simeq 1$–4 pursued further below, because if the low-redshift IDs were retained, they would not feature in the relevant redshift bins, while adoption of the long-wavelength redshift for these sources means that we do not include these sources in the sample of objects with reliable stellar masses. We also stress that only a small subset of these objects are likely lenses (five possible examples are highlighted in Fig. B2 available in the online version), but while a revised search for galaxy counterparts for the other sources might yield alternative counterparts with z_p consistent with z_{LW}, we prefer not to confuse subsequent analysis by the inclusion of what would be inevitably less reliable galaxy identifications.

As tabulated in Table 1, with this redshift refinement, the effective optical ID success rate for the most reliable ($p \leq 0.05$) IDs drops from 63 per cent to 51 per cent, while the overall ($p \leq 0.1$) ID success rate drops from 75 per cent to 58 per cent. However, while this reduces the number of reliably identified SCUBA-2 sources to $\simeq$ 50 per cent of the sample, this has the advantage or removing the most dubious identifications. Moreover, we stress that we retain redshift information for *every one* of the 106 SCUBA-2 sources, in the form of z_{LW} if neither z_{spec} nor a reliable value for z_p are available.

In Fig. B2 (available in the online version), we present 12 × 12 arcsec near-infrared postage-stamp images for every source, with the positions of all the IDs marked. In this figure, we give the source name in red if the optical ID was in fact subsequently rejected in the light of z_{LW}. It can be seen from this figure that at least some of these incorrect identifications are indeed due to galaxy–galaxy lensing (see the figure caption for details).

4.3 Redshift distribution

The differential redshift distribution for our SCUBA-2 galaxy sample is presented in Fig. 6. In the left-hand panel the black area depicts the redshift distribution for the sources with reliable optical IDs (and hence z_{spec} or z_p), while the histogram indicated in blue includes the additional unidentified SCUBA-2 sources with meaningful measurements of z_{LW}. Finally, the green histogram containing the green arrows indicates the impact of also including those sources for which only lower limits on their estimated redshifts could be derived from the long-wavelength photometry. The mean and median redshifts for the whole sample are $\bar{z} = 2.38 \pm 0.09$ (strictly speaking, a lower

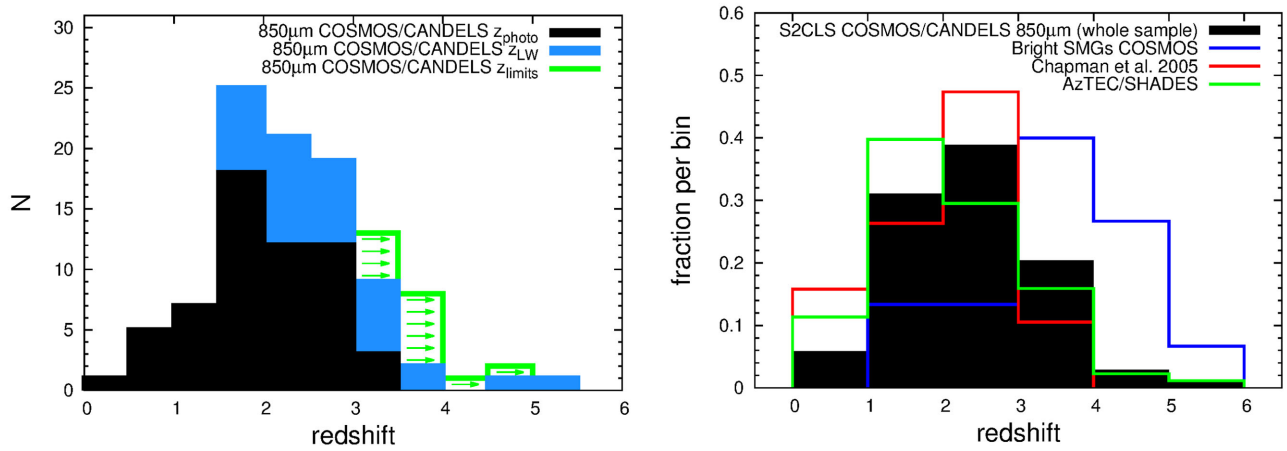

Figure 6. Left-hand panel: the redshift distribution of our full 106-source S2CLS 850 μm sample in the COSMOS field (Table A5). The black area shows the distribution for the robust optical identifications with spectroscopic or optical–infrared photometric redshifts, which has a mean redshift of $\bar{z} = 1.97 \pm 0.09$. The blue line depicts the redshift distribution of the enlarged sample which results from adding the SCUBA-2 sources which lack robust optical identifications, but which have reliable 'long-wavelength' redshifts ($z_{\rm LW}$). Finally, the additional histogram marked by the green arrows indicates the objects for which only lower limits on redshift could be derived from the long-wavelength photometry. Adopting these lower limits, the mean redshift for the whole sample is $\bar{z} = 2.38 \pm 0.09$. Right-hand panel: the redshift distribution for the whole S2CLS COSMOS sample overlaid with the redshift distributions derived by Chapman et al. (2005, $\bar{z} = 2.00 \pm 0.09$), and for the robust galaxy identifications in the AzTEC/SHADES survey presented by Michałowski et al. (2012a, $\bar{z} = 2.00 \pm 0.10$). In addition, we plot the redshift distribution of the sample of luminous (sub-)mm sources in the COSMOS field presented by Koprowski et al. (2014, $\bar{z} = 3.53 \pm 0.19$).

limit) and $z_{\rm med} = 2.21 \pm 0.06$, respectively, whereas, for the confirmed optical IDs with optical spectroscopic/photometric redshifts the corresponding numbers are $\bar{z} = 1.97 \pm 0.09$ and $z_{\rm med} = 1.96 \pm 0.07$. This shows that, as expected, the radio/infrared identification process biases the mean redshift towards lower redshifts, but in this case only by about $\simeq 10$ per cent in redshift. In addition, to make sure that our unidentified sources are in fact not spurious, which would manifest itself as them having low SNR values, we also plot in Fig. 7 the 850 μm flux as a function of redshift for the whole sample used here, colour-coded according to SNR. It can be clearly seen that the unidentified sources exhibit a wide range of SNRs and hence are most likely real.

In the right-hand panel of Fig. 6 we compare the redshift distribution of the deep 850 μm selected sample studied here with example redshift distributions from previous studies. Although our sample is somewhat deeper/fainter than the sub-mm samples studied previously by Chapman et al. (2005) and Michałowski et al. (2012a), the redshift distributions displayed by the optically identified subset of sources from each study are remarkably consistent; we find $\bar{z} = 1.97 \pm 0.09$, while Chapman et al. (2005) reported $\bar{z} = 2.00 \pm 0.09$, and Michałowski et al. (2012a) reported $\bar{z} = 2.00 \pm 0.10$.

While inclusion of our adopted values of $z_{\rm LW}$ for our unidentified sources moves the mean redshift up to at least $\bar{z} \simeq 2.4$, it is clear that the redshift distribution found here cannot be consistent with that found by Koprowski et al. (2014) for the subset of very bright sub-mm/mm sources in the COSMOS field (see also Smolcic et al. 2012), for which $\bar{z} = 3.53 \pm 0.19$. This is not due to any obvious inconsistency in redshift estimation techniques, as can be seen from Table 2 (discussed further below), and indeed the analysis methods used here are near identical to those employed by Koprowski et al. (2014). Rather, as discussed in Koprowski et al. (2014), there must either be a trend for the most luminous sub-mm/mm sources (i.e. $\bar{S}_{850\,\mu{\rm m}} \geq 8$ mJy) to lie at significantly higher redshifts than the more typical sources studied here, or the COSMOS bright source sample of Scott et al. (2008) imaged by Younger et al. (2007, 2009) and Smolcic et al. (2012) must be unusually dominated by a high-redshift overdensity in the COSMOS field.

4.4 Previous literature associations

Five of the sub-mm sources in our SCUBA-2 sample have been previously studied in some detail, and so, in Table 2, we compare our ID positions and redshifts with the pre-existing information. Four of these bright sources were previously the subject of interferometric mm/sub-mm observations, yielding robust optical identifications and photometric redshifts in good agreement with our results. The source separation for SC850-29 (2.03 arcsec) is perfectly plausible since this is the separation between the original AzTEC single-dish coordinate and our chosen ID. The small separations between the positions of our adopted IDs for SC850-6 and 31 and their mm/sub-mm interferometric centroids confirm the reliability of our ID selection. For SC850-1, the rather large source separation of 2.62 arcsec supports our rejection of the optical ID for this source. Finally, the rather large separation for SC850-14 clearly casts doubt on our adopted ID, but in this case $z_{\rm p}$ is very similar to $z_{\rm LW}$ (which, of course, is why we did not reject the ID) and so the final redshift distribution is unaffected by whether or not the ID is correct.

5 PHYSICAL PROPERTIES

5.1 Stellar masses and star formation rates

For the 58 SCUBA-2 sources for which we have secure optical identifications+redshifts (after the sample refinement discussed in Section 4.2) we were able to use the results of the SED fitting (used to determine $z_{\rm p}$) to obtain an estimate of the stellar mass, $M_\star$, for each galaxy. The derived stellar masses were based on the models of Bruzual & Charlot (2003) assuming double-burst star formation histories (see Michałowski et al. 2012b), and we assumed a Chabrier (2003) IMF.

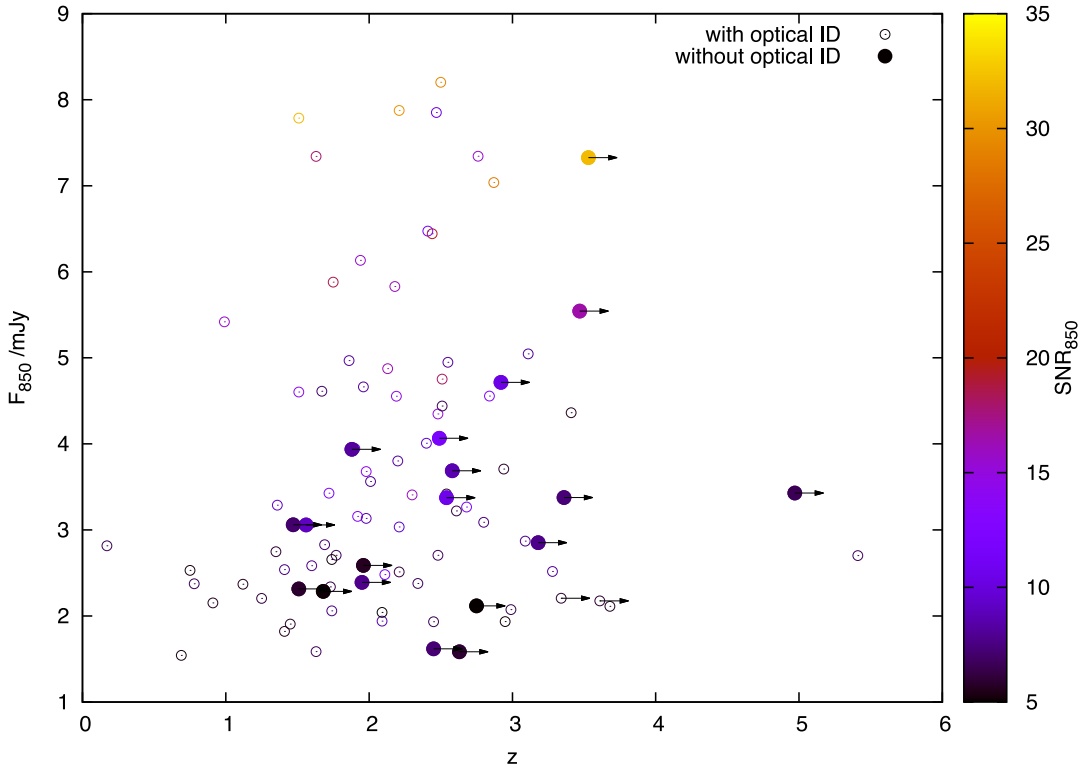

Figure 7. 850 μm flux density as a function of redshift for the whole SCUBA-2 850-μm sample used in this study. The open symbols show the 80 sources which possess optical IDs and the filled circles show the 26 sources that lack optical IDs, with arrows signifying lower limits on 'long-wavelength' redshifts. All the objects are colour-coded according to their 850 μm SNR. It can be seen that the galaxies that lack optical associations span a similar range in SNR to the optically identified sources. This suggests that the failure to uncover optical counterparts for these 26 sources is not due to them being spurious sub-mm detections, but instead suggests that either they lie at somewhat higher redshifts than the typical identified source, and/or that these unidentified SCUBA-2 sources are blends of individual fainter sources whose counterparts lie below the radio/24 μm detection threshold.

Table 2. Five sources in our sample that have been the subject of previous detailed study. Four of them (the ones with $z_{\rm prev}$) were previously followed up with the mm/sub-mm interferometry. The columns show respectively our ID, the source name from previous work (the full previous ID name for the AzTEC source is AzTEC J100025.23+022608.0), interferometric RA and Dec (or, in the case of the AzTEC source, single-dish coordinates), the separation between the interferometric position (except AzTEC) and the optical ID found in this work, our final redshifts (from Table A5), the redshift estimates from previous studies, and finally references. Where two references are given, the first one refers to the coordinates and the second to the previous redshift estimate (i.e. the source of $z_{\rm prev}$).

ID SC850-	ID_{other}	RA/deg	Dec/deg	Separation /arcsec	z	$z_{\rm prev}$	References
1	MM1	150.0650	2.2636	2.62	$3.30^{+0.22}_{-0.14}$	$3.10^{+0.50}_{-0.60}$	Aravena et al. (2010)
6	COSLA-35	150.0985	2.3653	0.13	$2.50^{+0.20}_{-0.15}$	$3.16^{+0.24}_{-0.26}$	Smolcic et al. (2012); Koprowski et al. (2014)
14	COSLA-8	150.1064	2.2523	2.76	$2.18^{+0.17}_{-0.13}$	$1.90^{+0.11}_{-0.22}$	Smolcic et al. (2012); Koprowski et al. (2014)
29	AzTEC	150.1051	2.4356	2.03	$2.41^{+0.24}_{-0.26}$	...	Scott et al. (2008)
31	COSLA-38	150.0525	2.2456	0.27	$2.47^{+0.08}_{-0.12}$	$2.44^{+0.12}_{-0.11}$	Smolcic et al. (2012)

We were also able to estimate the star formation rate, SFR, for each of these sources by using the average long-wavelength SED of the sub-mm galaxies from Michałowski et al. (2010), applied to the 850 μm flux-density of each source at the relevant photometric redshift, to estimate the far-infrared luminosity of each source.

The resulting SFRs are plotted against $M_\star$ in Fig. 8. In the main plot, for clarity we have confined attention to the sources with $z_{\rm p} > 1.5$ because, as shown in the inset plot, due to the impact of the negative K-correction at 850 μm, at $z > 1.5$ the flux-density limit of the current sample essentially equates to SFR $\simeq 100\,{\rm M}_\odot\,{\rm yr}^{-1}$ at all higher redshifts. In this plot, we also show the position of the MS of star-forming galaxies, as deduced at $z \simeq 2.5$ by Elbaz et al. (2011), and at $z > 1.5$ by Rodighiero et al. (2011). The sensitivity of our deep SCUBA-2 sample to values of SFR as low as $100\,{\rm M}_\odot\,{\rm yr}^{-1}$ means that, for objects with stellar masses $M_\star > 7 \times 10^{10}\,{\rm M}_\odot$, we are able for the first time to properly compare the positions of sub-mm-selected galaxies on the SFR:$M_\star$ plane with the MS in an unbiased manner.

5.2 Specific star formation rates

In Fig. 9, we collapse the information shown in Fig. 8 into distributions of specific SFR. The black histogram shows the distribution of sSFR for the whole robustly identified sample of SCUBA-2 sources at $z > 1.5$, but this can be subdivided by mass into the subsample with $M_\star > 7 \times 10^{10}\,{\rm M}_\odot$ (blue histogram) and the complementary

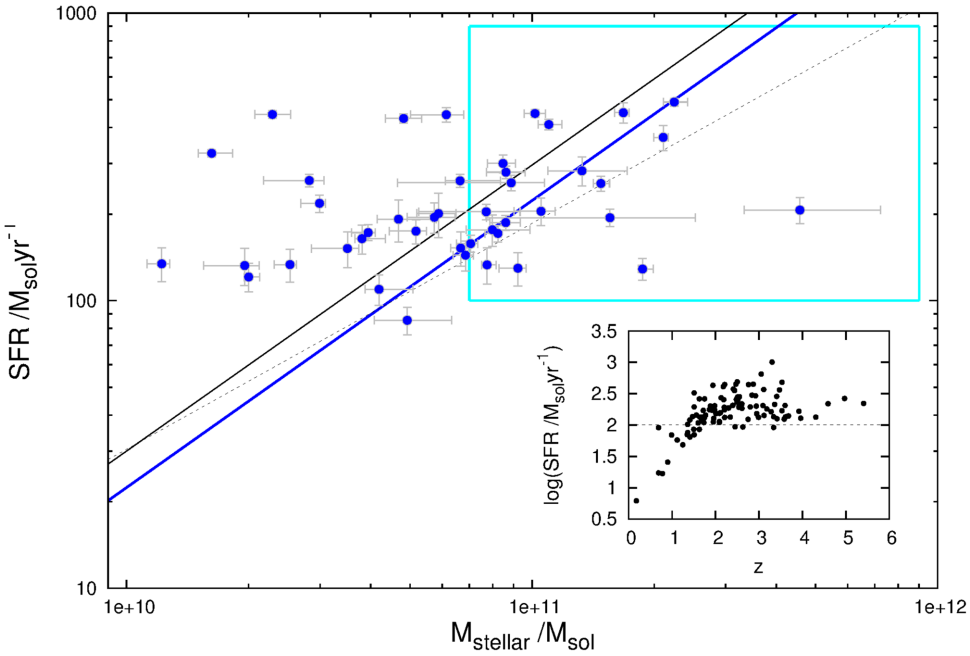

Figure 8. The star formation rate (SFR) as a function of stellar mass ($M_\star$) for the robustly identified SCUBA-2 sources with $z > 1.5$. As can be seen from the inset plot, due to the impact of the negative K-correction at 850 μm, for $z > 1.5$ the flux-density limit of the current sample essentially equates to SFR $\simeq$ 100 $M_\odot$ yr^{-1}. The black solid line in the main plot shows the position of the so-called main sequence (MS) of star-forming galaxies at $z \simeq 2.5$ as deduced by Elbaz et al. (2011), while the black dashed line depicts the MS at $z > 1.5$ as given by Rodighiero et al. (2011). The sensitivity of our deep SCUBA-2 sample to values of SFR as low as 100 $M_\odot$ yr^{-1} means that, for objects with stellar masses $M_\star > 7 \times 10^{10}$ $M_\odot$ yr^{-1} (i.e. inside the cyan rectangle), we are able for the first time to properly compare the positions of sub-mm-selected galaxies on the SFR:$M_\star$ plane with the MS in an unbiased manner. As shown in Fig. 9, we find that, confining our attention to $M_\star > 7 \times 10^{10}$ $M_\odot$ yr^{-1}, the SCUBA-2 sources display a Gaussian distribution in specific SFR peaking at sSFR = 2.25 ± 0.19 Gyr^{-1} (corresponding to the main sequence shown here by the blue solid line), demonstrating that the SCUBA-2 sources lie on the high-mass end of the normal star-forming MS at $z \simeq 2$.

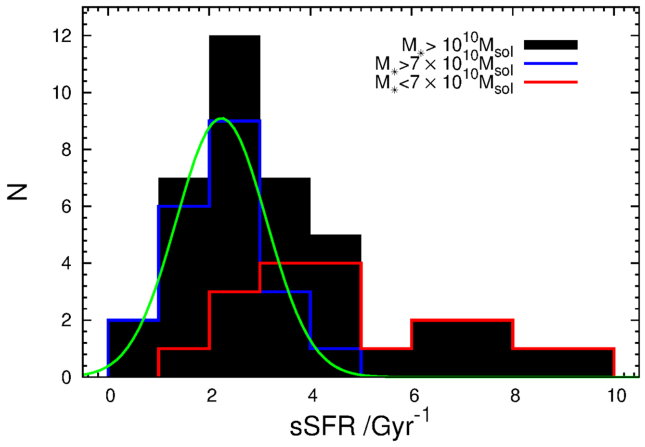

Figure 9. The distribution of specific star formation rate, sSFR, as derived from the values of SFR and $M_\star$ plotted in Fig. 8. The black histogram shows the distribution for the whole robustly identified sample of SCUBA-2 sources at $z > 1.5$, but this can be subdivided by mass into the subsample with $M_\star > 7 \times 10^{10}$ $M_\odot$ (blue histogram) and the complementary subsample of sources with $M_\star < 7 \times 10^{10}$ $M_\odot$ (red histogram). It can be seen that, for the high-mass sample, in which SFR is not biased by the effective flux-density limit of the deep SCUBA-2 survey, the distribution resembles closely a Gaussian peaked at sSFR = 2.25 Gyr^{-1} with σ = 0.89 Gyr^{-1}, as shown by the green curve. This demonstrates that, where their distribution on the SFR:$M_\star$ plane can now finally be probed in an unbiased manner, the SCUBA-2 galaxies lie on the MS of star-forming galaxies at $z \simeq 2$.

subsample of sources with $M_\star < 7 \times 10^{10}$ $M_\odot$ (red histogram). Referring back to Fig. 8, it can be seen that, at lower stellar masses, the measurement of sSFR is inevitably biased high by the effective SFR limit >100 $M_\odot$ yr^{-1}, and so it is difficult to tell if these SCUBA-2 sources genuinely lie above the MS, or if we are simply sampling the high-sSFR tail of the distribution around the MS. However, at $M_\star > 7 \times 10^{10}$ $M_\odot$ it is clear that the SFR limit would not produce a significantly biased sampling of the distribution of galaxies on the MS. In essence, because of the depth of the SCUBA-2 imaging, for sub-mm selected galaxies with $M_\star > 7 \times 10^{10}$ $M_\odot$ we should now be able to perform the first unbiased estimate of their sSFR at $z \simeq$ 1.5−3.

In fact, for the high-mass sub-sample, in which SFR is not biased by the effective flux-density limit of the deep SCUBA-2 survey, the distribution of sSFR resembles closely a Gaussian peaked at sSFR = 2.25 Gyr^{-1} with σ = 0.89 Gyr^{-1}. This Gaussian fit is shown by the green curve in Fig. 9, and is completely consistent with the normalization and scatter (≃0.25 dex) in the MS reported by Rodighiero et al. (2011).

Finally, to check whether we could be biased towards high-mass (and hence low sSFR) objects at high redshift, as a consequence of the flux-density limits of our optical/near-infrared catalogues, we plot the near-infrared (CANDELS H-band and UltraVISTA K_s-band) absolute magnitudes of our source IDs against redshift in Fig. 10. The measured values are generally not close to the detection limits of our catalogues, and therefore, we conclude that the sample is not biased against high sSFRs at high redshifts on account of an inability to detect low-mass galaxies.

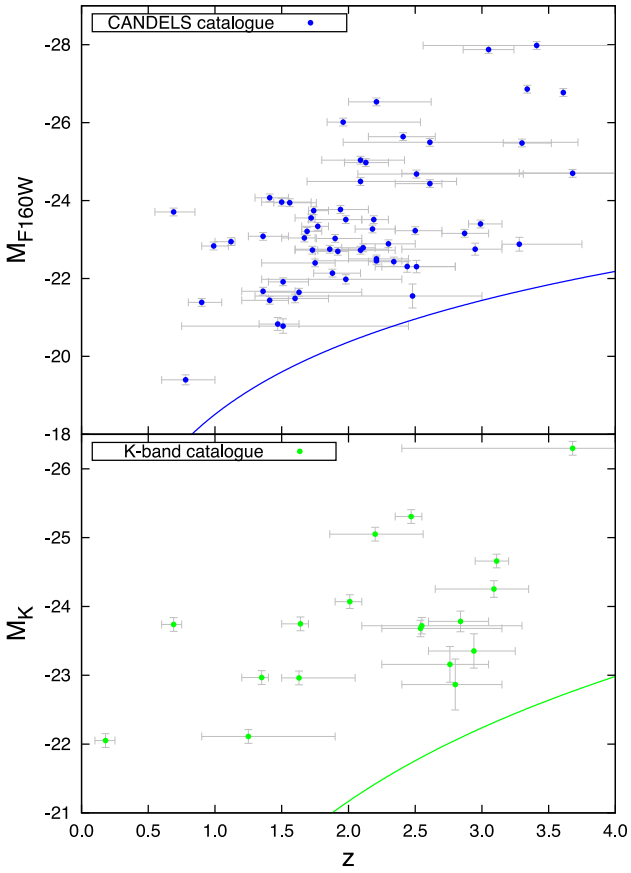

Figure 10. Absolute magnitude versus redshift for the secure SCUBA-2 near-infrared IDs as derived for the sources lying within the *HST* imaging (i.e. CANDELS *H*-band measurements; upper panel) and those lying outside the *HST* imaging (i.e. UltraVISTA K_s-band measurements; lower panel). The blue and green solid curves represent the detection limits of our CANDELS *H*-band and the UltraVISTA K_s-band-selected catalogues, respectively. It can be seen that virtually all the sources lie well above the detection limits, indicating that this our sample is not vulnerable to serious biases or incompleteness in stellar mass.

We conclude, therefore, within the stellar mass range where we are able to sample the distribution of sSFR in an unbiased way, the sub-mm sources uncovered from this deep SCUBA-2 850 μm image, display exactly the mean sSFR and scatter expected from galaxies lying on the high-mass end of the star-forming MS at $z \simeq 2$.

5.3 The 'MS' and its evolution

Given that the SCUBA-2 sources seem to, in effect, define the high-mass end of the star-forming MS of galaxies over the redshift range probed by our sample (i.e. $1.5 < z < 3$), it is of interest to explore how the inferred normalization and slope of the MS as derived here compares to that derived from other independent studies based on very different selection techniques over a wide range of redshifts.

Thus, in Fig. 11 we divide our (high-mass) sample into three redshift bins to place the inferred evolution of sSFR within the wider context of studies spanning virtually all of cosmic time (i.e. $0 < z < 8$).

The first obvious striking feature of Fig. 11 is that our new determination of average sSFR over the redshift range $1.5 < z < 3$ follows very closely the trend defined by the original studies of the MS undertaken by Noeske et al. (2007) and Daddi et al. (2007). Since such studies were based on very different samples, sampling lower stellar masses, this result also implies that we find no evidence for a high-mass turnover in the MS at these redshifts (i.e. a decline in sSFR, or change in the slope of the MS above some characteristic mass). Evidence for a decline in the slope of the MS above a stellar mass $\log(M^*/\mathrm{M}_\odot) \simeq 10.5$ has been presented by several authors (e.g. Whitaker et al. 2014; Tasca et al. 2015) but these results are based on optical/near-infrared studies, and suffer from two problems. First, as recently discussed by Johnston et al. (2015), the results of optically based studies depend crucially on how one selects star-forming galaxies, and colour selection can yield an apparent turn-over in the MS at high masses simply due to increased contamination from passive galaxies/bulges (see also Renzini & Peng 2015; Whitaker et al. 2015). Secondly, and more important, at the high SFRs of interest here, it is well known that SED fitting to optical–infrared data struggles to capture the total star formation rate because the vast majority of the star formation activity in high-mass galaxies is deeply obscured. It is therefore interesting that other recent studies of the MS based on far-infrared/sub-mm data also find no evidence for a high mass turnover in the MS at high redshift; for example Schreiber et al. (2015), from their *Herschel* stacking study of the MS, report that any evidence for a flattening of the MS above $\log(M^*/\mathrm{M}_\odot) \simeq 10.5$ becomes less prominent with increasing redshift and vanishes by $z \simeq 2$.

As is clear from Fig. 8, the present study does not provide sufficient dynamic range to enable a new measurement of the precise value and redshift evolution of the slope of the MS (see Speagle et al. 2014 for results from a compilation of 25 studies). Nevertheless, the advantages of sub-mm selection for an unbiased study of the high-mass end of the MS are clear (i.e. no contamination from passive galaxies, and a complete census of dust-enshrouded star formation), and our results show that the slope of the MS must remain close to unity up to stellar masses $M^* \simeq 2 \times 10^{11}\,\mathrm{M}_\odot$ at $z \simeq 2$–3. We note that it is sometimes claimed that studies of the MS based on far-IR or sub-mm-selected samples yield vastly different determinations of the SFR–M^* relation from the MS (e.g. Rodighiero et al. 2014), but it needs to be understood that this is because previous studies based on such samples did not reach sufficient sensitivity in SFR (for individual objects) to properly sample the MS at high redshift. As emphasized in Section 5.2, and in Fig. 8, even the deepest ever 850 μm survey analysed here only enables us to properly explore the MS at the very highest masses, due to the effective SFR sensitivity limit; clearly, the sources detected in the present study at lower masses are outliers from the MS, and can only provide indirect information of the scatter in the MS at masses of a few $\times 10^{10}\,\mathrm{M}_\odot$, rather than its normalization.

Finally, looking to higher redshifts, Fig. 11 shows that the present study does not provide useful information on characteristic sSFR beyond $z \simeq 3$, but also demonstrates that the trend indicated here over $1.5 < z < 3$ extends naturally out to our previous determination of sSFR in very high-redshift sub-mm/mm galaxies at $z \simeq 5$ (Koprowski et al. 2014). There is currently considerable debate over the normalization of the MS at $z \simeq 4$, due in large part to uncertainty over the impact of nebular emission lines on the estimation of stellar masses (see e.g. Stark et al. 2013; Smit et al. 2014). However, the sub-mm studies of high-mass star-forming galaxies are clearly consistent with the results of several existing studies (e.g. Steinhardt et al. 2014), and (despite their supposedly extreme star formation rates) sub-mm-selected galaxies provide additional support for the presence of a 'knee' in the evolution of sSFR around $z \simeq 2$ (as

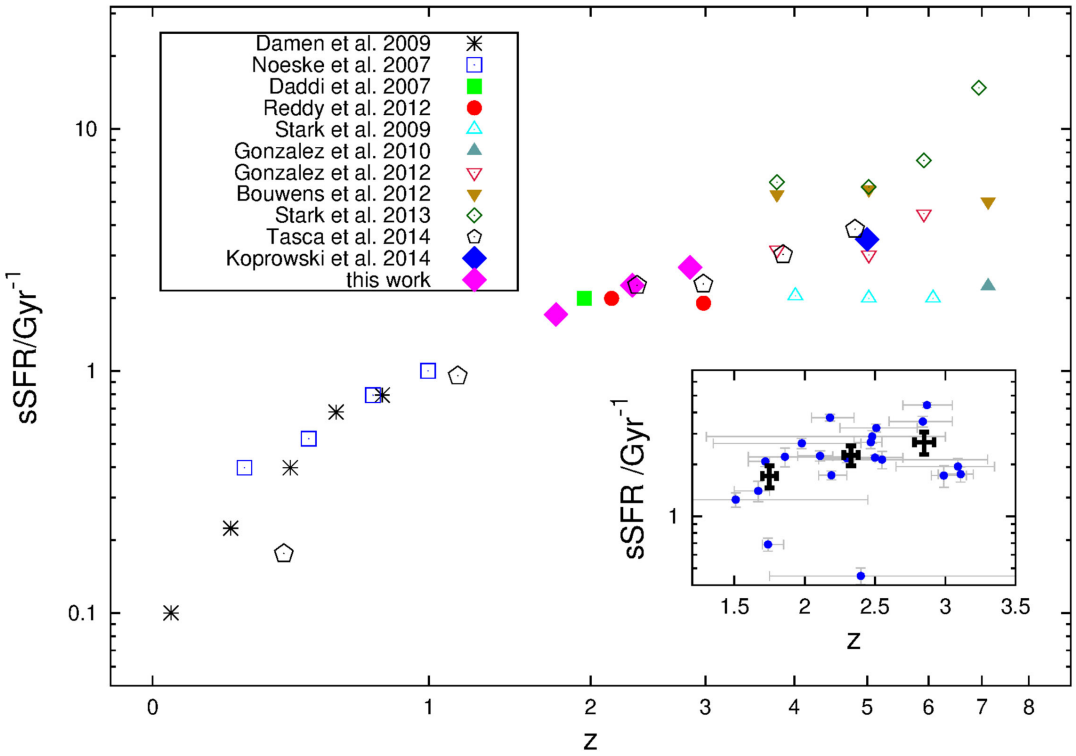

Figure 11. Mean sSFR as a function of the redshift. The results of this work (inset plot with the mean values represented by black points with thick error bars) calculated using the unbiased sample (from inside the cyan rectangle in Fig. 8) are shown by the magenta diamonds. It can be seen that the evolution of characteristic sSFR (≡to the normalization of the MS) inferred from the SCUBA-2 galaxies is in excellent accord with the results from many other studies.

originally suggested by the results of González et al. 2010, 2012). The ability of theoretical models of galaxy formation to reproduce this transition remains the subject of continued debate, with smooth cold accretion on to dark matter haloes leading to expectations that sSFR should rise $\propto(1+z)^{2.5}$ (Dekel et al. 2009, 2013; Faucher-Giguère, Keres & Ma 2011; Rodríguez-Puebla et al. 2016), and a range of hydrodynamical and semi-analytic models of galaxy formation yielding predictions of characteristic sSFR at $z \simeq 2$ that fall short of the results shown in Fig. 11 by a factor of 2–6 (see discussion in Johnston et al. 2015, and references therein). However, in Fig. 12 we show that when the redshift axis is re-cast in terms of cosmic time, there is really no obvious feature in the evolution of characteristic sSFR. Rather, the challenge for theoretical models is to reproduce the apparently simple fact that $\log_{10}$sSFR is a linear function of the age of the Universe, at least out to the highest redshifts probed to date.

6 SUMMARY

We have investigated the multiwavelength properties of the galaxies selected from the deepest 850 μm survey undertaken to date with SCUBA-2 on the JCMT. This deep 850-μm imaging was taken in parallel with deep 450 μm imaging in the very best observing conditions as part of the S2CLS. A total of 106 sources ($>5\sigma$) were uncovered at 850 μm from an area of ≃150 arcmin^2 in the centre of the COSMOS/UltraVISTA/CANDELS field, imaged to a typical depth of $\sigma_{850} \simeq 0.25$ mJy. Aided by radio, mid-IR and 450-μm positional information, we established statistically robust galaxy counterparts for 80 of these sources (≃75 per cent).

By combining the optical–infrared photometric redshifts, $z_{\rm p}$, of these galaxies with independent 'long-wavelength' estimates of redshift, $z_{\rm LW}$ (based on *Herschel*/SCUBA-2/VLA photometry), we have been able to refine the list of robust galaxy identifications. This approach has also enabled us to complete the redshift content of the whole sample, yielding $\bar{z} = 2.38 \pm 0.09$, a mean redshift comparable with that derived from all but the brightest previous sub-mm samples.

Because our new deep 850-μm-selected galaxy sample reaches flux densities equivalent to star formation rates SFR ≃ 100 M$_\odot$ yr^{-1}, we have been able to confirm that sub-mm galaxies form the high-mass end of the MS of star-forming galaxies at $z > 1.5$ (with a mean specific SFR of sSFR $= 2.25 \pm 0.19$ Gyr^{-1} at $z \simeq 2.5$). Our results are consistent with no significant flattening of the MS towards high stellar masses at these redshifts (i.e. SFR continues $\propto M_*$), suggesting that reports of such flattening are based on contamination by passive galaxies/bulges, and/or underestimates of dust-enshrouded star formation activity in massive star-forming galaxies. However, our findings contribute to the growing evidence that average sSFR rises only slowly at high redshift, from sSFR ≃ 2 Gyr^{-1} at $z \simeq 2$ to sSFR ≃ 4 Gyr^{-1} at $z \simeq 5$. These results are consistent with a rather simple evolution of global characteristic sSFR, in which $\log_{10}$sSFR is a linear function of the age of the Universe, at least out to the highest redshifts probed to date.

ACKNOWLEDGEMENTS

MPK acknowledges the support of the UK Science and Technology Facilities Council. JSD and RAAB acknowledge the support of the European Research Council via the award of an Advanced Grant (PI J. Dunlop). JSD also acknowledges the contribution of the EC FP7 SPACE project ASTRODEEP (Ref. No: 312725). MJM acknowledges the support of the UK Science and Technology

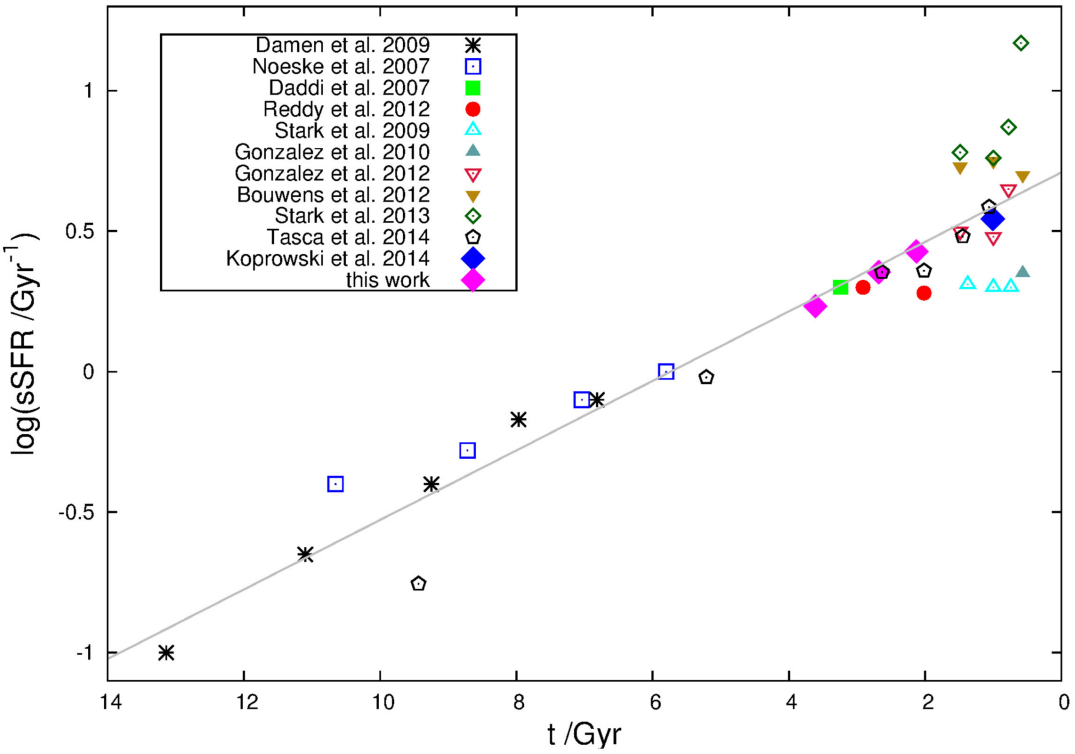

Figure 12. Mean sSFR as a function of cosmic time. Data/symbols are as in Fig. 11. The straight-line fit to the data has the form $\log_{10}(\mathrm{sSFR/Gyr^{-1}}) = -0.12(t/\mathrm{Gyr}) + 0.71$.

Facilities Council, and the FWO Pegasus Marie Curie Fellowship. MC acknowledges the support of the UK Science and Technology Facilities Council via an Advanced Fellowship.

The JCMT has historically been operated by the Joint Astronomy Centre on behalf of the Science and Technology Facilities Council of the United Kingdom, the National Research Council of Canada and the Netherlands Organization for Scientific Research. Additional funds for the construction of SCUBA-2 were provided by the Canada Foundation for Innovation. This work is based in part on data products from observations made with ESO Telescopes at the La Silla Paranal Observatories under ESO programme ID 179.A-2005 and on data products produced by TERAPIX and the Cambridge Astronomy survey Unit on behalf of the UltraVISTA consortium. This work is based in part on observations obtained with MegaPrime/MegaCam a joint project of CFHT and CEA/DAPNIA, at the CFHT which is operated by the National Research Council (NRC) of Canada, the Institut National des Science de l'Univers of the Centre National de la Recherche Scientifique (CNRS) of France and the University of Hawaii. This work is based in part on data products produced at TERAPIX and the Canadian Astronomy Data Centre as part of the CFHTLS, a collaborative project of NRC and CNRS. This work is based in part on observations made with the NASA/ESA *HST*, which is operated by the Association of Universities for Research in Astronomy, Inc., under NASA contract NAS5-26555. This work is also based in part on observations made with the *Spitzer Space Telescope*, which is operated by the Jet Propulsion Laboratory, California Institute of Technology under NASA contract 1407, as well as the observations made with ESO Telescopes at the La Silla or Paranal Observatories under programme ID 175.A-0839. *Herschel* is an ESA space observatory with science instruments provided by European-led Principal Investigator consortia and with important participation from NASA. We thank the staff of the Subaru telescope for their assistance with the z'-band imaging utilized here. This research has made use of the NASA/IPAC Infrared Science Archive, which is operated by the Jet Propulsion Laboratory, California Institute of Technology, under contract with the National Aeronautics and Space Administration.

REFERENCES

Aravena M., Younger J. D., Fazio G. G., Gurwell M., Espada D., Bertoldi F., Capak P., Wilner D., 2010, ApJ, 719, L15
Ashby M. L. et al., 2013, ApJ, 768, 80
Austermann J. E. et al., 2010, MNRAS, 401, 160
Barger A. J., Cowie L. L., Sanders D. B., Fulton E., Taniguchi Y., Sato Y., Kawara K., Okuda H., 1998, Nature, 394, 238
Bertin E., Arnouts S., 1996, A&AS, 117, 393
Bertoldi F. et al., 2000, A&A, 360, 92
Biggs A. D. et al., 2011, MNRAS, 413, 2314
Bintley D. et al., 2014, Proc. SPIE, 9153, 915303
Bolzonella M., Miralles J.-M., Pelló R., 2000, A&A, 363, 476
Bouwens R. J. et al., 2012, ApJ, 754, 83
Bouwens R. J. et al., 2015, ApJ, 803, 34
Bowler R. A. A. et al., 2012, MNRAS, 426, 2772
Bowler R. A. A. et al., 2014, MNRAS, 440, 2810
Bowler R. A. A. et al., 2015, MNRAS, 452, 1817
Brammer G. B. et al., 2012, ApJS, 200, 13
Bruzual G., Charlot S., 2003, MNRAS, 344, 1000
Calzetti D., Armus L., Bohlin R. C., Kinney A. L., Koornneef J., Storchi-Bergmann T., 2000, ApJ, 533, 682
Capak P. et al., 2008, ApJ, 681, L53
Caputi K. I. et al., 2006, ApJ, 637, 727
Chabrier G., 2003, PASP, 115, 763
Chapin E. L., Berry D. S., Gibb A. G., Jenness T., Scott D., Tilanus R. P. J., Economou F., Holland W. S., 2013, MNRAS, 430, 2545
Chapman S. C., Blain A. W., Smail I., Ivison R. J., 2005, ApJ, 622, 772

Cirasuolo M. et al., 2007, MNRAS, 380, 585
Cirasuolo M., McLure R. J., Dunlop J. S., Almaini O., Foucaud S., Simpson C., 2010, MNRAS, 401, 1166
Coe D. et al., 2013, ApJ, 762, 32
Combes F. et al., 2012, A&A, 538, L4
Condon J. J., 1992, ARA&A, 30, 575
Coppin K. E. K. et al., 2006, MNRAS, 372, 1621
Coppin K. E. K. et al., 2009, MNRAS, 395, 1905
Cox P. et al., 2011, ApJ, 740, 63
Daddi E. et al., 2007, ApJ, 670, 156
Daddi E. et al., 2009a, ApJ, 694, 1517
Daddi E., Dannerbauer H., Krips M., Walter F., Dickinson M., Elbaz D., Morrison G. E., 2009b, ApJ, 695, L176
Damen M., Forster Schreiber N. M., Franx M., Labbé I., Toft S., van Dokkum P. G., Wuyts S., 2009, ApJ, 705, 617
Dekel A. et al., 2009, Nature, 457, 451
Dekel A., Zolotov A., Tweed D., Cacciato M., Ceverino D., Primack J. R., 2013, MNRAS, 435, 999
Dempsey J. T. et al., 2013, MNRAS, 430, 2543
Diolaiti E., Bendinelli O., Bonaccini D., Close L., Currie D., Parmeggiani G., 2000, A&AS, 147, 335
Dole H. et al., 2006, A&A, 451, 417
Dunlop J. S., 2013, Astrophys. Space Sci. Libr., 396, 223
Dunlop J. S., Peacock J. A., Savage A., Lilly S. J., Heasley J. N., Simon A. J. N., 1989, MNRAS, 238, 1171
Dunlop J. S. et al., 2004, MNRAS, 350, 769
Dunlop J. S. et al., 2010, MNRAS, 408, 2022
Dye S. et al., 2008, MNRAS, 386, 1107
Eales S., Lilly S., Gear W., Dunne L., Bond J. R., Hammer F., Le Févre O., Crampton D., 1999, ApJ, 515, 518
Elbaz D. et al., 2010, A&A, 518, L29
Elbaz D. et al., 2011, A&A, 533, 119
Ellis R. S. et al., 2013, ApJ, 763, L7
Faucher-Giguère C.-A., Keres D., Ma C.-P., 2011, MNRAS, 417, 2982
Finkelstein S. L. et al., 2015, ApJ, 810, 71
Geach J. E. et al., 2013, MNRAS, 432, 53
González V., Labbé I., Bouwens R. J., Illingworth G., Franx M., Kriek M., Brammer G. B., 2010, ApJ, 713, 115
González V., Bouwens R. J., Labbé I., Illingworth G., Oesch P., Franx M., Magee D., 2012, ApJ, 755, 148
Greve T. R., Ivison R. J., Bertoldi F., Stevens J. A., Dunlop J. S., Lutz D., Carilli C. L., 2004, MNRAS, 354, 779
Griffin M. J. et al., 2010, A&A, 518, L3
Grogin N. A. et al., 2011, ApJS, 197, 35
Gwyn S. D. J., 2012, AJ, 143, 38
Hainline L. J., Blain A. W., Smail I., Alexander D. M., Armus L., Chapman S. S., Ivison R. J., 2011, ApJ, 740, 96
Hodge J. A. et al., 2013, ApJ, 768, 91
Holland W. S. et al., 1999, MNRAS, 303, 659
Holland W. S. et al., 2013, MNRAS, 430, 2513
Hughes D. H. et al., 1998, Nature, 394, 241
Ishigaki M., Kawamata R., Ouchi M., Oguri M., Shimasaku K., Ono Y., 2015, ApJ, 799, 12
Ivison R. J. et al., 2007, MNRAS, 380, 199
Johnston R., Vaccari M., Jarvis M., Smith M., Giovannoli E., Haussler B., Prescott M., 2015, MNRAS, 453, 2540
Karim A. et al., 2011, ApJ, 730, 61
Karim A. et al., 2013, MNRAS, 432, 2
Knudsen K. K., Neri R., Kneib J.-P., van der Werf P. P., 2010, A&A, 496, 45
Koprowski M. P., Dunlop J. S., Michałowski M. J., Cirasuolo M., Bowler R. A. A., 2014, MNRAS, 444, 117
Le Floc'h E. et al., 2009, ApJ, 703, 222
Leja J., van Dokkum P., Franx M., Whitaker K. E., 2015, ApJ, 798, 115
Lilly S. J. et al., 2007, ApJS, 172, 70
Lutz D. et al., 2011, A&A, 532, 90
McCracken H. J. et al., 2012, A&A, 544, 156
McLeod D. J., McLure R. J., Dunlop J. S., Robertson B. E., Ellis R. S., Targett T. T., 2015, MNRAS, 450, 3032
McLure R. J. et al., 2013, MNRAS, 432, 2696
Madau P., 1995, ApJ, 441, 18
Madau P., Ferguson H. C., Dickinson M. E., Giavalisco M., Steidel C. C., Fruchter A., 1996, MNRAS, 283, 1388
Michałowski M. J., Hjorth J., Watson D., 2010, A&A, 514, 67
Michałowski M. J. et al., 2012a, MNRAS, 426, 1845
Michałowski M. J., Dunlop J. S., Cirasuolo M., Hjorth J., Hayward C. C., Watson D., 2012b, A&A, 541, 85
Michałowski M. J., Hayward C. C., Dunlop J. S., Bruce V. A., Cirasuolo M., Cullen F., Hernquist L., 2014, A&A, 571, 75
Mitchell P. D., Lacey C. G., Cole S., Baugh C. M., 2014, MNRAS, 444, 2637
Noeske K. G. et al., 2007, ApJ, 660, L43
Oesch P. A. et al., 2014, ApJ, 786, 108
Oke J. B., 1974, ApJS, 27, 21
Oke J. B., Gunn J. E., 1983, ApJ, 266, 713
Oliver S. J. et al., 2010, MNRAS, 405, 2279
Oliver S. J. et al., 2012, MNRAS, 424, 1614
Ono Y., Ouchi M., Kurono Y., Momose R., 2014, ApJ, 795, 5
Peng C. Y., Ho L. C., Impey C. D., Rix H. W., 2002, AJ, 124, 266
Pilbratt G. L. et al., 2010, A&A, 518, L1
Poglitsch A. et al., 2010, A&A, 518, L2
Reddy N. A., Pettini M., Steidel C. C., Shapley A. E., Erb D. K., Law D. R., 2012, ApJ, 754, 25
Renzini A., Peng Y.-J., 2015, ApJ, 801, L29
Riechers D. A. et al., 2010, ApJ, 720, L131
Riechers D. A., 2013, Nature, 502, 459
Rodighiero G. et al., 2011, ApJ, 739, L40
Rodighiero G. et al., 2014, MNRAS, 443, 19
Rodríguez-Puebla A., Primack J. R., Behroozi P., Faber S. M., 2016, MNRAS, 455, 2592
Roseboom I. G. et al., 2013, MNRAS, 436, 430
Salmon B. et al., 2015, ApJ, 799, 183
Sanders D. B. et al., 2007, ApJS, 172, 86
Santini P. et al., 2009, A&A, 504, 751
Schinerrer E. et al., 2010, ApJS, 188, 384
Schreiber C. et al., 2015, A&A, 575, 74
Scott S. E. et al., 2002, MNRAS, 331, 817
Scott S. E., Dunlop J. S., Serjeant S., 2006, MNRAS, 370, 1057
Scott K. S. et al., 2008, MNRAS, 385, 2225
Scott K. S. et al., 2012, MNRAS, 423, 575
Skelton R. E. et al., 2014. ApJS, 214, 24
Smail I., Ivison R. J., Blain A. W., 1997, ApJ, 490, L5
Smit R. et al., 2014, ApJ, 784, 58
Smolcic V. et al., 2012, A&A, 548, 4
Speagle J. S., Steinhardt C. L., Capak P. L., Silverman J. D., 2014, ApJS, 214, 15
Stark D. P., Ellis R. S., Bunker A., Bundy K., Targett T., Benson A., Lacy M., 2009, ApJ, 697, 1493
Stark D. P., Schenker M. A., Ellis R., Robertson B., McLure R., Dunlop J., 2013, ApJ, 763, 129
Steidel C. C., Giavalisco M., Pettini M., Dickinson M., Adelberger K. L., 1996 ApJ, 462, L17
Steinhardt C. L. et al., 2014, ApJ, 791, L25
Taniguchi Y. et al., 2007, ApJS, 172, 9
Tasca L. A. M. et al., 2015, A&A, 581, 54
Walter F. et al., 2012, Nature, 486, 233
Wardlow J. L. et al., 2011, MNRAS, 415, 1479
Weiss A. et al., 2009, ApJ, 707, 1201
Weiss A. et al., 2013, ApJ, 767, 88
Whitaker K. E. et al., 2014, ApJ, 795, 104
Whitaker K. E. et al., 2015, ApJ, 811, L12
Younger J. D. et al., 2007, ApJ, 671, 1531
Younger J. D. et al., 2009, ApJ, 704, 803

SUPPORTING INFORMATION

Additional Supporting Information may be found in the online version of this article:

APPENDIX B.
(http://www.mnras.oxfordjournals.org/lookup/suppl/doi:10.1093/mnras/stw564/-/DC1).

Please note: Oxford University Press is not responsible for the content or functionality of any supporting materials supplied by the authors. Any queries (other than missing material) should be directed to the corresponding author for the article.

APPENDIX: DATA TABLES

In this appendix, we provide tables detailing: (i) the sub-mm properties of the deep 106-source 850 μm-selected SCUBA-2 sample utilized in this study, (ii) the results of the galaxy counterpart identification process, (iii) the optical–infrared photometry for the galaxy identifications and (iv) the estimated redshifts and derived physical properties of the sub-mm galaxies.

Table A1. The basic properties of the 106-source SCUBA-2 850 μm-selected sample. The penultimate column gives the SCUBA-2 colour where, if the significance of the 450 μm detection is less than 2σ, the SCUBA-2 colour is based on a 450 μm limit with $S_{450} < S_{450} + 2\sigma$. The flag given in the final column indicates whether the 450 μm flux density was taken from 450 μm catalogue (1) or simply measured at the 850 μm position (0); the latter measurement was adopted if no 450 μm-selected source with $S_{450} > 4\sigma$ was found within 6 arcsec of the 850 μm source position).

ID	RA_{850} (deg)	DEC_{850} (deg)	S_{850} (mJy)	ΔS_{850} (mJy)	SNR_{850}	S_{450} (mJy)	ΔS_{450} (mJy)	SNR_{450}	S_{850}/S_{450}	flag
1	150.065 18	2.264 12	15.64	0.38	41.69	26.99	2.38	11.34	0.58	1
2	150.099 85	2.297 72	10.20	0.28	36.82	17.74	1.77	10.00	0.58	1
3	150.100 79	2.334 99	7.33	0.23	32.02	10.32	1.41	7.34	0.71	1
4	150.105 49	2.313 27	7.79	0.24	31.96	23.42	1.53	15.35	0.33	1
5	150.143 20	2.356 07	7.88	0.26	29.98	19.71	1.54	12.78	0.40	1
6	150.098 33	2.365 68	8.20	0.28	29.20	22.81	1.80	12.71	0.36	1
7	150.098 47	2.321 62	7.04	0.25	28.44	16.66	1.53	10.88	0.42	1
8	150.098 20	2.260 61	6.44	0.33	19.32	14.89	2.13	6.98	0.43	1
9	150.078 09	2.281 68	5.88	0.32	18.56	15.45	2.03	7.62	0.38	1
10	150.153 90	2.328 33	4.75	0.26	18.17	11.15	1.55	7.17	0.43	1
11	150.042 64	2.373 71	7.34	0.41	17.85	23.66	2.87	8.23	0.31	1
12	150.109 96	2.258 32	5.54	0.34	16.55	8.91	2.13	4.18	0.62	1
13	150.085 12	2.290 50	4.87	0.30	16.25	12.79	1.97	6.50	0.38	1
14	150.106 92	2.252 18	5.83	0.36	16.03	23.81	2.38	9.99	0.24	1
15	150.117 17	2.330 26	3.41	0.21	15.95	6.53	1.31	4.99	0.52	1
16	150.056 33	2.373 63	5.42	0.35	15.53	24.31	2.39	10.17	0.22	1
17	150.207 99	2.382 97	7.34	0.47	15.50	15.66	2.68	5.83	0.47	1
18	150.163 93	2.372 74	6.13	0.40	15.43	31.22	1.96	15.90	0.20	1
19	150.112 58	2.376 33	4.35	0.29	15.14	9.91	1.84	5.37	0.44	1
20	150.150 24	2.364 57	4.55	0.31	14.46	13.31	1.76	7.56	0.34	1
21	150.098 73	2.311 18	3.68	0.26	13.89	9.08	1.62	5.61	0.41	1
22	150.057 27	2.293 52	4.60	0.33	13.88	12.83	2.19	5.87	0.36	1
23	150.122 83	2.360 81	3.16	0.24	13.36	10.41	1.50	6.94	0.30	1
24	150.109 37	2.294 55	3.43	0.27	12.58	11.88	1.74	6.84	0.29	1
25	150.037 91	2.340 79	4.56	0.36	12.49	9.20	2.48	3.71	0.50	0
26	150.080 11	2.340 91	3.27	0.27	11.97	10.70	1.77	6.06	0.31	1
27	150.174 16	2.352 83	4.07	0.34	11.83	8.82	2.01	4.38	0.46	1
28	150.121 69	2.341 75	2.48	0.21	11.59	10.56	1.30	8.13	0.23	1
29	150.105 35	2.435 31	6.47	0.57	11.31	18.98	3.59	5.28	0.34	1
30	150.144 89	2.376 45	3.37	0.32	10.54	8.44	1.78	4.75	0.40	1
31	150.052 50	2.244 77	7.85	0.76	10.40	14.21	5.63	2.52	0.55	0
32	150.066 41	2.412 64	4.72	0.46	10.29	6.49	3.18	2.04	0.73	0
33	150.041 53	2.280 39	4.01	0.42	9.53	6.73	2.60	2.59	0.60	0
34	150.135 14	2.399 48	3.03	0.32	9.39	11.12	1.94	5.73	0.27	1
35	150.167 42	2.299 50	3.29	0.35	9.36	11.12	1.91	5.84	0.30	1
36	150.082 08	2.415 90	3.95	0.43	9.11	10.88	2.91	3.74	0.36	0
37	150.068 12	2.276 18	3.06	0.34	9.08	11.70	2.08	5.62	0.26	1
38	150.076 20	2.380 36	3.14	0.35	8.87	12.41	2.27	5.46	0.25	1
39	150.093 22	2.246 97	3.69	0.43	8.63	11.67	2.83	4.12	0.32	1
40	150.105 70	2.326 38	1.94	0.23	8.52	7.87	1.38	5.72	0.25	1
41	150.128 88	2.284 74	2.47	0.29	8.48	0.96	1.91	0.50	>0.51	0
42	150.028 19	2.347 02	3.80	0.45	8.36	0.76	2.97	0.26	>0.57	0
43	150.172 14	2.241 49	4.97	0.59	8.35	3.39	3.87	0.88	>0.45	0
44	150.136 63	2.233 05	4.66	0.57	8.23	2.28	3.48	0.66	>0.50	0
45	150.127 44	2.387 98	2.52	0.31	8.21	4.50	1.87	2.41	0.56	0

Table A1 – *continued*

ID	RA_{850} (deg)	DEC_{850} (deg)	S_{850} (mJy)	ΔS_{850} (mJy)	SNR_{850}	S_{450} (mJy)	ΔS_{450} (mJy)	SNR_{450}	S_{850}/S_{450}	flag
46	150.106 06	2.428 44	3.94	0.48	8.14	14.48	3.09	4.69	0.27	1
47	150.048 63	2.252 78	4.95	0.62	8.04	3.14	4.64	0.68	>0.40	0
48	150.022 27	2.288 99	5.05	0.63	8.00	16.71	3.63	4.60	0.30	1
49	150.157 25	2.357 41	2.58	0.33	7.83	10.44	1.84	5.67	0.25	1
50	150.081 03	2.362 98	2.39	0.31	7.79	0.75	1.95	0.38	>0.51	0
51	150.035 51	2.285 37	3.56	0.46	7.76	1.63	2.76	0.59	>0.50	0
52	150.036 93	2.319 59	2.85	0.37	7.72	1.68	2.47	0.68	>0.43	0
53	150.187 80	2.322 96	2.54	0.33	7.64	15.59	1.84	8.46	0.16	1
54	150.043 07	2.299 82	2.87	0.36	7.63	10.50	2.36	4.45	0.27	1
55	150.134 42	2.370 59	2.06	0.27	7.55	10.13	1.68	6.04	0.20	1
56	150.050 05	2.385 74	3.09	0.41	7.50	7.69	2.95	2.61	0.40	0
57	150.156 14	2.419 84	3.38	0.45	7.30	2.77	2.72	1.02	>0.41	0
58	150.107 09	2.344 44	1.62	0.22	7.24	4.98	1.36	3.66	0.32	0
59	150.183 68	2.388 79	2.83	0.39	7.22	10.40	2.14	4.86	0.27	1
60	150.191 99	2.273 00	3.25	0.46	7.12	0.68	2.95	0.23	>0.49	0
61	150.054 19	2.396 15	3.06	0.43	7.10	8.03	3.08	2.61	0.38	0
62	150.166 89	2.236 08	4.61	0.65	7.08	8.03	4.13	1.95	>0.28	0
63	150.076 08	2.398 21	2.70	0.39	6.85	0.89	2.62	0.34	>0.44	0
64	150.130 04	2.315 05	1.59	0.23	6.82	8.63	1.45	5.95	0.18	1
65	150.091 67	2.398 37	2.71	0.40	6.78	11.02	2.49	4.42	0.25	1
66	150.174 80	2.401 68	2.70	0.40	6.76	9.29	2.18	4.27	0.29	1
67	150.111 57	2.404 09	2.38	0.35	6.73	3.22	2.27	1.42	>0.31	0
68	150.130 19	2.253 38	2.37	0.36	6.68	7.01	2.29	3.06	0.34	0
69	150.155 07	2.243 89	3.10	0.47	6.63	−2.98	3.02	−0.99	>0.51	0
70	150.024 90	2.296 68	3.43	0.52	6.63	3.49	3.16	1.11	>0.35	0
71	150.072 11	2.238 37	4.44	0.67	6.62	−6.58	4.78	−1.38	>0.46	0
72	150.065 12	2.329 22	1.93	0.29	6.60	8.04	2.09	3.84	0.24	0
73	150.209 10	2.355 67	2.82	0.43	6.60	18.21	2.40	7.57	0.15	1
74	150.071 15	2.306 05	2.07	0.32	6.55	2.53	2.21	1.15	>0.30	0
75	150.159 43	2.296 48	2.34	0.35	6.40	10.40	1.96	5.32	0.22	1
76	150.182 68	2.336 01	2.01	0.32	6.31	−0.32	1.83	−0.17	>0.55	0
77	150.071 48	2.423 07	3.22	0.51	6.28	3.97	3.60	1.10	>0.29	0
78	150.099 11	2.405 16	2.51	0.39	6.23	5.50	2.49	2.21	0.46	0
79	150.042 49	2.327 99	2.20	0.35	6.19	3.49	2.36	1.48	>0.27	0
80	150.136 24	2.261 35	2.06	0.34	6.05	−0.66	2.16	−0.30	>0.48	0
81	150.126 30	2.413 79	2.21	0.37	5.98	1.27	2.35	0.54	>0.37	0
82	150.152 86	2.320 11	1.59	0.27	5.93	3.65	1.60	2.29	0.43	0
83	150.025 72	2.313 35	2.75	0.46	5.93	6.50	2.92	2.22	0.42	0
84	150.111 86	2.408 79	2.18	0.37	5.92	−1.58	2.36	−0.67	>0.46	0
85	150.119 84	2.417 67	2.32	0.39	5.87	7.06	2.52	2.80	0.33	0
86	150.052 00	2.305 54	1.91	0.33	5.87	2.38	2.23	1.07	>0.28	0
87	150.224 09	2.356 46	3.71	0.64	5.83	−1.10	3.16	−0.35	>0.59	0
88	150.053 89	2.276 30	2.11	0.37	5.68	0.83	2.27	0.37	>0.39	0
89	150.161 78	2.268 14	2.15	0.38	5.67	13.81	2.32	5.96	0.16	1
90	150.054 76	2.258 01	2.59	0.46	5.63	−5.87	3.14	−1.87	>0.41	0
91	150.070 11	2.290 22	1.82	0.32	5.60	3.47	2.07	1.67	>0.24	0
92	150.059 80	2.400 55	2.37	0.43	5.57	4.56	3.01	1.52	>0.22	0
93	150.057 51	2.428 10	4.36	0.78	5.57	14.01	5.47	2.56	0.31	0
94	150.061 99	2.379 70	1.95	0.35	5.53	−2.09	2.40	−0.87	>0.41	0
95	150.016 47	2.320 95	3.42	0.62	5.51	3.28	3.58	0.92	>0.33	0
96	150.108 07	2.423 69	2.39	0.45	5.36	1.88	2.82	0.67	>0.32	0
97	150.095 48	2.286 61	1.53	0.29	5.31	0.28	1.88	0.15	>0.38	0
98	150.160 77	2.341 68	1.54	0.29	5.29	9.34	1.73	5.40	0.17	1
99	150.209 84	2.312 58	2.53	0.48	5.29	15.46	2.73	5.67	0.16	1
100	150.218 41	2.344 89	2.79	0.53	5.25	1.80	2.72	0.66	>0.38	0
101	150.148 54	2.254 58	2.01	0.38	5.22	−2.33	2.44	−0.95	>0.41	0
102	150.037 20	2.272 15	2.66	0.51	5.21	14.78	3.25	4.55	0.18	1
103	150.086 04	2.380 99	1.94	0.36	5.18	13.00	2.28	5.70	0.15	1
104	150.141 08	2.423 86	2.29	0.45	5.10	15.70	2.83	5.55	0.15	1
105	150.164 71	2.409 32	2.04	0.40	5.04	4.68	2.27	2.06	0.44	0
106	150.208 93	2.350 22	2.12	0.42	5.02	3.52	2.40	1.47	>0.25	0

Table A2. The results of the radio/mid-infrared statistical identification process described in Section 3. The columns give the SCUBA-2 source number, the positions of the adopted optical ID, the VLA 1.4 GHz coordinates (where a radio ID exists), and the relevant mid-infrared and radio flux densities, angular offsets (from the SCUBA-2 850 μm position), and corrected probabilities, p, that each association could have occurred by chance (given the depth of the supporting data, the relevant number counts, and the counterpart search radius). If a given ID is listed more than once, the counterpart with the lowest p-value was treated as a correct association. The robust IDs ($p \leq 0.05$) are shown in bold, the more tentative IDs ($0.05 < p \leq 0.1$) in italics, and the sources for which the optical/near-infrared IDs were rejected on the basis of the $z_{\rm p} - z_{\rm LW}$ comparison (see Section 4.2) are marked with asterisks.

ID SC850-	RA_{opt} (deg)	DEC_{opt} (deg)	RA_{VLA} (deg)	DEC_{VLA} (deg)	$S_{8.0}$ (μJy)	$dist_{8.0}$ (arcsec)	$p_{8.0}$	S_{24} (mJy)	$dist_{24}$ (arcsec)	p_{24}	S_{VLA} (mJy)	$dist_{VLA}$ (arcsec)	p_{VLA}
1*	150.064 60	2.264 05	–	–	18.88	2.47	*0.062*	0.13	2.18	**0.036**	–	–	–
2*	150.100 14	2.297 13	150.099 94	2.297 21	35.00	2.23	**0.032**	0.16	1.42	**0.016**	0.187	1.85	**0.001**
4	150.105 46	2.312 85	150.105 35	2.312 84	24.71	1.57	**0.026**	0.23	0.65	**0.003**	0.058	1.62	**0.002**
5	150.143 04	2.355 85	150.143 23	2.356 02	14.21	0.66	**0.011**	0.14	0.40	**0.002**	0.517	0.20	**0.000**
6	150.098 54	2.365 36	150.098 65	2.365 38	31.79	1.35	**0.016**	0.24	1.20	**0.007**	0.043	1.60	**0.002**
7	150.098 66	2.320 81	–	–	15.93	3.16	*0.092*	0.12	2.30	**0.041**	–	–	–
8	150.097 90	2.260 01	–	–	9.47	1.91	*0.070*	–	–	–	–	–	–
9	150.079 11	2.281 80	–	–	–	–	–	0.33	1.35	**0.003**	–	–	–
9	–	–	–	–	27.09	2.21	**0.040**	0.31	1.97	**0.012**	–	–	–
9	–	–	–	–	14.09	3.85	0.116	0.30	4.05	**0.035**	–	–	–
10	150.153 74	2.328 00	–	–	19.41	1.36	**0.026**	–	–	–	–	–	–
11	150.043 26	2.373 48	150.043 18	2.373 57	20.86	2.15	**0.047**	0.27	1.30	**0.004**	0.100	2.03	**0.002**
13*	150.084 40	2.290 49	–	–	59.24	2.71	**0.027**	0.42	2.43	**0.010**	–	–	–
14	150.106 41	2.251 61	150.106 35	2.251 61	26.43	2.94	*0.059*	0.58	2.53	**0.007**	0.112	2.89	**0.003**
15	150.117 54	2.329 96	–	–	14.97	1.69	**0.044**	0.16	1.33	**0.009**	–	–	–
16	150.056 57	2.373 75	150.056 49	2.373 83	107.95	0.88	**0.003**	0.46	0.78	**0.001**	0.088	0.90	**0.001**
17	150.207 97	2.383 08	–	–	21.93	0.71	**0.008**	0.07	0.15	**0.001**	–	–	–
18	150.163 57	2.372 42	150.163 51	2.372 51	34.47	1.64	**0.020**	0.56	1.41	**0.003**	0.138	1.72	**0.001**
19	150.112 55	2.376 54	–	–	10.47	0.76	**0.018**	0.10	0.93	**0.013**	–	–	–
20	150.150 26	2.364 14	–	–	30.45	1.54	**0.021**	0.21	1.00	**0.007**	–	–	–
21	150.098 67	2.311 18	–	–	11.97	0.37	**0.005**	0.18	0.90	**0.007**	–	–	–
22	150.057 06	2.292 86	–	–	14.36	2.45	*0.073*	0.16	2.09	**0.028**	–	–	–
23	150.122 94	2.360 96	–	–	12.93	0.61	**0.011**	0.23	0.65	**0.002**	–	–	–
24	150.109 09	2.294 33	–	–	21.57	1.37	**0.024**	0.22	0.64	**0.002**	–	–	–
25	150.037 29	2.340 57	150.037 40	2.340 71	9.31	2.50	*0.096*	0.07	1.69	**0.040**	0.062	1.86	**0.003**
26	150.079 37	2.340 56	150.079 25	2.340 52	13.55	3.04	*0.096*	0.16	2.82	**0.042**	0.061	3.38	**0.005**
26	–	–	–	–	–	–	–	0.18	2.68	**0.022**	–	–	–
28	150.121 81	2.341 31	–	–	10.69	1.76	*0.059*	0.10	2.09	**0.042**	–	–	–
29*	150.105 25	2.434 99	–	–	13.36	1.21	**0.030**	0.08	0.89	**0.014**	–	–	–
31	150.052 48	2.245 55	–	–	37.59	2.89	**0.043**	0.38	1.50	**0.003**	–	–	–
33	150.040 98	2.280 63	–	–	11.41	1.89	*0.062*	0.08	2.74	*0.068*	–	–	–
34*	150.135 13	2.399 42	150.134 95	2.399 30	14.60	0.38	**0.004**	0.17	0.32	**0.001**	0.056	0.96	**0.001**
35	150.167 71	2.298 76	–	–	16.71	2.85	*0.080*	0.32	2.62	**0.018**	–	–	–
36*	150.081 87	2.415 56	–	–	–	–	–	0.64	0.72	**0.001**	–	–	–
37	150.068 11	2.275 69	–	–	29.14	1.92	**0.030**	0.45	1.53	**0.004**	–	–	–
38	150.075 27	2.379 40	–	–	–	–	–	0.13	1.28	**0.017**	–	–	–
40*	150.105 31	2.325 90	–	–	–	–	–	0.06	3.12	**0.050**	–	–	–
42*	150.027 54	2.345 77	–	–	–	–	–	0.16	4.32	*0.069*	–	–	–
43	150.171 86	2.240 70	–	–	18.90	2.87	*0.074*	0.21	2.77	**0.032**	–	–	–
44*	150.137 02	2.232 22	150.136 58	2.232 52	46.55	2.98	**0.038**	0.22	2.39	**0.024**	0.045	1.94	**0.003**
45	150.127 15	2.387 86	–	–	12.64	1.21	**0.031**	0.06	0.98	**0.020**	–	–	–
46	150.105 90	2.428 79	–	–	–	–	–	0.13	1.99	**0.033**	–	–	–
47	150.048 25	2.251 44	–	–	–	–	–	0.13	4.21	**0.047**	–	–	–
48	150.021 41	2.288 67	–	–	20.33	3.16	*0.079*	–	–	–	–	–	−−
49	150.157 47	2.358 03	–	–	–	–	–	0.19	3.38	**0.047**	–	–	–
51	150.036 52	2.286 17	–	–	–	–	–	0.10	3.63	**0.049**	–	–	–
53	150.187 63	2.322 50	–	–	46.19	1.80	**0.018**	0.24	1.73	**0.013**	–	–	–
54	150.042 41	2.299 85	–	–	19.09	2.46	*0.061*	0.09	2.47	*0.056*	–	–	–
55	150.133 54	2.370 42	–	–	15.81	3.32	*0.097*	0.10	2.10	**0.027**	–	–	–
56	150.050 02	2.386 07	–	–	–	–	–	0.05	1.15	**0.026**	–	–	–
59	150.184 97	2.388 94	–	–	–	–	–	0.11	4.48	*0.088*	–	–	–
61	150.053 97	2.395 90	–	–	11.07	1.39	**0.042**	0.16	0.73	**0.006**	–	–	–
62	150.166 91	2.235 82	–	–	20.71	0.89	**0.013**	0.37	0.69	**0.002**	–	–	–
63*	150.076 72	2.398 60	–	–	12.09	2.56	*0.086*	–	–	–	–	–	–
64	150.130 74	2.314 08	–	–	–	–	–	0.18	4.05	*0.059*	–	–	–
65*	150.091 56	2.399 04	–	–	58.66	2.46	**0.024**	0.16	2.19	**0.018**	–	–	–

Table A2 *– continued*

ID SC850-	RA_{opt} (deg)	DEC_{opt} (deg)	RA_{VLA} (deg)	DEC_{VLA} (deg)	$S_{8.0}$ (μJy)	$dist_{8.0}$ (arcsec)	$p_{8.0}$	S_{24} (mJy)	$dist_{24}$ (arcsec)	p_{24}	S_{VLA} (mJy)	$dist_{VLA}$ (arcsec)	p_{VLA}
66	150.175 61	2.401 59	–	–	27.26	2.72	*0.052*	0.16	2.34	**0.034**	–	–	–
67	150.111 32	2.403 20	–	–	9.76	3.36	0.121	0.11	3.22	*0.067*	–	–	–
68	150.130 01	2.252 69	–	–	10.88	2.59	*0.092*	0.18	2.63	**0.034**	–	–	–
71*	150.071 94	2.238 67	–	–	–	–	–	0.08	2.14	*0.050*	–	–	–
72*	150.064 56	2.329 03	–	–	111.50	2.24	**0.012**	0.29	1.99	**0.013**	–	–	–
73	150.209 62	2.355 25	150.209 55	2.355 31	1446.07	2.32	**0.001**	1.46	2.07	**0.001**	0.273	2.09	**0.001**
74	150.070 66	2.305 14	–	–	10.24	3.65	0.130	0.05	3.68	*0.096*	–	–	–
75	150.159 33	2.296 80	–	–	8.45	1.30	**0.047**	0.07	1.47	**0.034**	–	–	–
77*	150.070 27	2.422 97	–	–	–	–	–	0.10	3.72	**0.050**	–	–	–
78	150.099 44	2.404 87	–	–	10.07	1.28	**0.042**	0.10	1.08	**0.010**	–	–	–
79	150.041 18	2.328 13	–	–	–	–	–	0.13	3.85	**0.043**	–	–	–
79	–	–	–	–	43.14	3.81	*0.059*	–	–	–	–	–	–
81*	150.125 82	2.413 54	–	–	–	–	–	–	–	–	–	–	–
83	150.024 92	2.312 87	–	–	12.00	3.40	0.127	0.16	4.09	**0.041**	–	–	–
84*	150.111 54	2.409 57	–	–	19.59	3.09	*0.086*	0.04	3.05	*0.086*	–	–	–
86	150.051 66	2.305 85	–	–	73.38	1.75	**0.012**	0.34	1.67	**0.008**	–	–	–
87	150.224 34	2.356 44	–	–	11.10	0.74	**0.017**	0.09	0.98	**0.016**	–	–	–
88*	150.054 56	2.275 35	–	–	82.07	4.21	**0.044**	0.27	3.35	**0.019**	–	–	–
88	–	–	–	–	31.33	2.41	**0.043**	–	–	–	–	–	–
89	150.162 55	2.268 08	–	–	–	–	–	0.07	1.39	**0.032**	–	–	–
91	150.070 60	2.289 20	–	–	12.83	4.01	0.149	0.18	4.25	**0.040**	–	–	–
92	150.059 16	2.399 82	–	–	21.66	3.63	0.100	0.09	4.54	*0.064*	–	–	–
93*	150.057 85	2.427 23	–	–	44.59	3.25	**0.049**	0.07	3.23	*0.088*	–	–	–
95	150.016 40	2.320 96	–	–	14.17	0.27	**0.003**	–	–	–	–	–	–
98	150.161 86	2.340 92	–	–	46.07	4.71	*0.081*	0.31	4.68	**0.043**	–	–	–
99	150.210 20	2.311 67	150.210 13	2.311 68	93.38	3.50	**0.031**	0.91	3.11	**0.005**	0.227	3.41	**0.003**
102	150.037 45	2.271 86	150.036 70	2.270 98	20.84	1.32	**0.026**	–	–	–	0.075	1.03	**0.001**
102	–	–	150.037 38	2.271 94	61.12	4.82	*0.068*	0.71	3.56	**0.009**	0.080	4.57	**0.008**
103	150.085 14	2.381 95	–	–	–	–	–	0.39	2.45	**0.008**	–	–	–
105*	150.164 26	2.408 81	–	–	12.05	2.25	*0.088*	0.27	2.36	**0.012**	–	–	–

Table A3. The optical–infrared photometry for the SCUBA-2 identifications that lie within the CANDELS *HST* imaging. The table gives CFHTLS optical, Subaru z'-band, UltraVISTA near-infrared, IRAC mid-infrared and *HST* AB magnitudes as measured through 3 arcsec-diameter apertures. Errors are the 1σ values, with a minimum adopted error of 0.1 mag.

ID	RA	DEC	u	g	r	i	z	Y	J	H	Ks	3.6 μm	4.5 μm	$F125W$	$F160W$
1	150.064 60	2.264 05	25.02 ± 0.10	24.60 ± 0.10	24.17 ± 0.10	23.65 ± 0.10	23.09 ± 0.10	22.67 ± 0.10	22.30 ± 0.10	21.85 ± 0.10	21.51 ± 0.10	20.97 ± 0.10	20.77 ± 0.10	22.24 ± 0.10	21.80 ± 0.10
2	150.100 14	2.297 13	24.51 ± 0.10	22.47 ± 0.10	20.96 ± 0.10	20.31 ± 0.10	20.05 ± 0.10	19.81 ± 0.10	19.51 ± 0.10	19.18 ± 0.10	18.87 ± 0.10	19.62 ± 0.10	19.77 ± 0.10	19.49 ± 0.10	19.19 ± 0.10
4	150.105 46	2.312 85	–	26.97 ± 0.40	26.50 ± 0.38	25.99 ± 0.31	25.51 ± 0.17	24.43 ± 0.27	24.75 ± 0.43	23.21 ± 0.17	22.43 ± 0.10	21.44 ± 0.10	21.06 ± 0.10	24.05 ± 0.12	23.29 ± 0.10
5	150.143 04	2.355 85	–	26.78 ± 0.34	26.04 ± 0.25	25.50 ± 0.20	25.63 ± 0.19	24.90 ± 0.41	24.38 ± 0.31	24.08 ± 0.37	22.97 ± 0.16	22.24 ± 0.10	21.83 ± 0.10	24.39 ± 0.16	23.72 ± 0.10
6	150.098 54	2.365 36	–	–	26.46 ± 0.36	26.25 ± 0.40	26.05 ± 0.27	–	24.77 ± 0.44	23.47 ± 0.21	22.54 ± 0.11	21.21 ± 0.10	20.82 ± 0.10	24.68 ± 0.21	23.32 ± 0.10
7	150.098 66	2.320 81	–	26.09 ± 0.18	25.39 ± 0.14	25.22 ± 0.15	25.25 ± 0.13	–	24.70 ± 0.41	23.56 ± 0.23	23.09 ± 0.18	22.36 ± 0.10	21.86 ± 0.10	24.39 ± 0.16	23.75 ± 0.10
8	150.097 90	2.260 01	26.61 ± 0.29	25.85 ± 0.14	25.32 ± 0.13	24.93 ± 0.12	24.91 ± 0.10	–	24.54 ± 0.36	24.10 ± 0.38	23.73 ± 0.32	23.37 ± 0.11	23.21 ± 0.14	24.52 ± 0.18	24.18 ± 0.15
9	150.079 11	2.281 80	27.29 ± 0.54	26.35 ± 0.23	26.41 ± 0.35	25.31 ± 0.17	24.98 ± 0.10	24.66 ± 0.33	23.87 ± 0.19	23.01 ± 0.14	22.59 ± 0.11	21.59 ± 0.10	21.35 ± 0.10	23.68 ± 0.10	23.20 ± 0.10
10	150.153 74	2.328 00	–	–	–	–	–	–	–	–	23.49 ± 0.26	22.29 ± 0.10	21.77 ± 0.10	–	24.25 ± 0.16
13	150.084 40	2.290 49	23.55 ± 0.10	23.11 ± 0.10	22.91 ± 0.10	22.47 ± 0.10	22.11 ± 0.10	22.14 ± 0.10	21.69 ± 0.10	21.23 ± 0.10	20.70 ± 0.10	20.10 ± 0.10	19.89 ± 0.10	21.55 ± 0.10	21.15 ± 0.10
14	150.106 41	2.251 61	–	26.67 ± 0.30	26.27 ± 0.30	25.50 ± 0.20	25.11 ± 0.12	–	23.69 ± 0.16	22.86 ± 0.12	21.95 ± 0.10	20.70 ± 0.10	20.31 ± 0.10	23.84 ± 0.10	22.92 ± 0.10
15	150.117 54	2.329 96	–	–	26.35 ± 0.33	26.09 ± 0.34	25.77 ± 0.21	–	24.65 ± 0.39	23.36 ± 0.19	22.55 ± 0.11	21.62 ± 0.10	21.29 ± 0.10	24.34 ± 0.16	23.44 ± 0.10
16	150.056 57	2.373 75	25.14 ± 0.10	24.66 ± 0.10	24.01 ± 0.10	23.22 ± 0.10	22.57 ± 0.10	22.25 ± 0.10	21.78 ± 0.10	21.33 ± 0.10	20.71 ± 0.10	20.16 ± 0.10	19.82 ± 0.10	21.74 ± 0.10	21.24 ± 0.10
18	150.163 57	2.372 42	25.12 ± 0.10	24.32 ± 0.10	23.98 ± 0.10	23.65 ± 0.10	23.45 ± 0.10	23.29 ± 0.10	22.57 ± 0.10	22.06 ± 0.10	21.48 ± 0.10	20.75 ± 0.10	20.48 ± 0.10	22.49 ± 0.10	22.11 ± 0.10
19	150.112 55	2.376 54	–	–	–	–	–	–	–	–	24.00 ± 0.41	22.46 ± 0.10	21.93 ± 0.10	–	24.98 ± 0.31
20	150.150 26	2.364 14	26.01 ± 0.17	25.19 ± 0.10	24.71 ± 0.10	24.71 ± 0.10	24.32 ± 0.10	23.53 ± 0.12	23.38 ± 0.12	22.65 ± 0.10	21.86 ± 0.10	20.95 ± 0.10	20.67 ± 0.10	23.45 ± 0.10	22.69 ± 0.10
21	150.098 67	2.311 18	–	–	–	–	26.59 ± 0.45	–	–	–	23.20 ± 0.20	22.08 ± 0.10	21.72 ± 0.10	24.89 ± 0.26	23.95 ± 0.12
22	150.057 06	2.292 86	–	–	–	–	–	–	–	23.97 ± 0.33	22.91 ± 0.15	21.72 ± 0.10	21.24 ± 0.10	25.42 ± 0.42	24.43 ± 0.19
23	150.122 94	2.360 96	–	27.04 ± 0.43	26.32 ± 0.32	25.66 ± 0.23	25.07 ± 0.11	–	23.76 ± 0.17	23.51 ± 0.22	22.27 ± 0.10	21.35 ± 0.10	21.04 ± 0.10	23.60 ± 0.10	23.15 ± 0.10
24	150.109 09	2.294 33	26.25 ± 0.21	25.22 ± 0.10	25.02 ± 0.10	24.17 ± 0.10	23.73 ± 0.10	23.32 ± 0.10	22.46 ± 0.10	21.92 ± 0.10	21.47 ± 0.10	20.77 ± 0.10	20.52 ± 0.10	22.50 ± 0.10	22.00 ± 0.10
26	150.079 37	2.340 56	25.53 ± 0.11	24.29 ± 0.10	23.76 ± 0.10	23.45 ± 0.10	23.28 ± 0.10	23.15 ± 0.10	22.78 ± 0.10	22.27 ± 0.10	21.89 ± 0.10	21.59 ± 0.10	21.37 ± 0.10	22.72 ± 0.10	22.23 ± 0.10
28	150.121 81	2.341 31	26.87 ± 0.37	25.47 ± 0.10	25.23 ± 0.12	25.35 ± 0.17	24.83 ± 0.10	25.10 ± 0.50	23.74 ± 0.17	23.20 ± 0.17	22.64 ± 0.12	22.29 ± 0.10	22.22 ± 0.10	23.82 ± 0.10	23.31 ± 0.10
29	150.105 25	2.434 99	24.44 ± 0.10	23.59 ± 0.10	22.75 ± 0.10	21.82 ± 0.10	21.33 ± 0.10	21.30 ± 0.10	21.07 ± 0.10	20.81 ± 0.10	20.49 ± 0.10	20.42 ± 0.10	20.92 ± 0.10	21.07 ± 0.10	20.81 ± 0.10
34	150.135 13	2.399 42	21.72 ± 0.10	20.55 ± 0.10	20.07 ± 0.10	19.80 ± 0.10	19.83 ± 0.10	19.76 ± 0.10	19.74 ± 0.10	19.78 ± 0.10	20.04 ± 0.10	20.70 ± 0.10	20.81 ± 0.10	19.74 ± 0.10	19.69 ± 0.10
35	150.167 71	2.298 76	–	–	–	–	25.79 ± 0.21	25.17 ± 0.53	24.02 ± 0.22	23.19 ± 0.16	22.04 ± 0.10	20.96 ± 0.10	20.70 ± 0.10	23.91 ± 0.10	23.25 ± 0.10
36	150.081 87	2.415 56	26.65 ± 0.30	24.45 ± 0.10	23.73 ± 0.10	23.43 ± 0.10	23.39 ± 0.10	23.45 ± 0.11	23.38 ± 0.12	22.78 ± 0.11	22.82 ± 0.14	23.01 ± 0.10	22.98 ± 0.11	23.12 ± 0.10	22.79 ± 0.10
37	150.068 11	2.275 69	23.96 ± 0.10	22.51 ± 0.10	22.82 ± 0.10	22.82 ± 0.10	22.32 ± 0.10	22.01 ± 0.10	21.54 ± 0.10	21.11 ± 0.10	20.81 ± 0.10	–	–	21.79 ± 0.10	21.35 ± 0.10
38	150.075 27	2.379 40	26.25 ± 0.21	25.24 ± 0.10	24.77 ± 0.10	24.33 ± 0.10	23.94 ± 0.10	23.80 ± 0.15	22.95 ± 0.10	22.54 ± 0.10	21.65 ± 0.10	21.37 ± 0.10	21.22 ± 0.10	22.98 ± 0.10	22.42 ± 0.10
40	150.105 31	2.325 90	26.12 ± 0.18	25.78 ± 0.13	25.33 ± 0.13	24.58 ± 0.10	24.39 ± 0.10	24.22 ± 0.22	24.42 ± 0.32	23.17 ± 0.16	22.93 ± 0.15	22.39 ± 0.10	22.07 ± 0.10	23.85 ± 0.10	23.35 ± 0.10
43	150.171 86	2.240 70	–	–	–	25.98 ± 0.31	25.86 ± 0.23	–	24.08 ± 0.23	22.94 ± 0.13	22.15 ± 0.10	21.02 ± 0.10	20.84 ± 0.10	23.87 ± 0.10	23.01 ± 0.10

Table A3 – *continued*

ID	RA	DEC	u	g	r	i	z	Y	J	H	Ks	3.6 μm	4.5 μm	$F125W$	$F160W$
44	150.137 02	2.232 22	21.67 ± 0.10	20.68 ± 0.10	20.43 ± 0.10	20.14 ± 0.10	20.20 ± 0.10	20.08 ± 0.10	20.01 ± 0.10	19.95 ± 0.10	19.93 ± 0.10	20.60 ± 0.10	20.83 ± 0.10	20.01 ± 0.10	19.89 ± 0.10
45	150.127 15	2.387 86	–	–	26.18 ± 0.28	26.13 ± 0.35	25.69 ± 0.20	–	24.96 ± 0.53	–	23.24 ± 0.21	23.35 ± 0.11	22.86 ± 0.10	24.99 ± 0.28	24.38 ± 0.18
46	150.105 90	2.428 79	24.71 ± 0.10	23.68 ± 0.10	23.45 ± 0.10	23.94 ± 0.10	23.45 ± 0.10	22.96 ± 0.10	23.05 ± 0.10	22.73 ± 0.11	22.91 ± 0.15	–	–	23.96 ± 0.11	23.66 ± 0.10
49	150.157 47	2.358 03	26.82 ± 0.35	25.97 ± 0.16	25.58 ± 0.16	25.53 ± 0.20	25.23 ± 0.13	24.84 ± 0.39	24.91 ± 0.50	23.94 ± 0.33	23.09 ± 0.18	22.22 ± 0.10	21.89 ± 0.10	24.21 ± 0.14	23.87 ± 0.11
53	150.187 63	2.322 50	25.71 ± 0.13	25.13 ± 0.10	24.50 ± 0.10	23.71 ± 0.10	22.95 ± 0.10	22.22 ± 0.10	21.57 ± 0.10	20.90 ± 0.10	20.38 ± 0.10	19.61 ± 0.10	19.48 ± 0.10	21.55 ± 0.10	20.95 ± 0.10
55	150.133 54	2.370 42	24.99 ± 0.10	24.51 ± 0.10	24.25 ± 0.10	23.94 ± 0.10	23.54 ± 0.10	23.29 ± 0.10	22.35 ± 0.10	21.86 ± 0.10	21.30 ± 0.10	20.77 ± 0.10	20.59 ± 0.10	22.37 ± 0.10	21.85 ± 0.10
59	150.184 97	2.388 94	24.79 ± 0.10	24.14 ± 0.10	23.99 ± 0.10	23.63 ± 0.10	23.39 ± 0.10	23.11 ± 0.10	22.49 ± 0.10	22.25 ± 0.10	22.06 ± 0.10	21.67 ± 0.10	21.53 ± 0.10	22.60 ± 0.10	22.30 ± 0.10
61	150.053 97	2.395 90	–	25.38 ± 0.10	24.49 ± 0.10	25.12 ± 0.14	24.14 ± 0.10	24.28 ± 0.23	23.93 ± 0.20	23.63 ± 0.24	22.99 ± 0.16	21.48 ± 0.10	21.34 ± 0.10	24.91 ± 0.26	24.31 ± 0.17
62	150.166 91	2.235 82	26.48 ± 0.26	25.74 ± 0.13	25.51 ± 0.15	24.76 ± 0.10	24.47 ± 0.10	23.85 ± 0.16	23.02 ± 0.10	22.33 ± 0.10	21.67 ± 0.10	20.71 ± 0.10	20.46 ± 0.10	22.97 ± 0.10	22.44 ± 0.10
63	150.076 72	2.398 60	–	–	–	26.44 ± 0.47	25.79 ± 0.22	–	–	23.42 ± 0.20	22.75 ± 0.13	22.00 ± 0.10	21.61 ± 0.10	24.57 ± 0.19	23.84 ± 0.11
64	150.130 74	2.314 08	–	–	–	26.45 ± 0.48	26.01 ± 0.26	–	24.55 ± 0.36	23.37 ± 0.19	23.05 ± 0.17	21.75 ± 0.10	21.36 ± 0.10	24.48 ± 0.18	23.77 ± 0.10
65	150.091 56	2.399 04	23.49 ± 0.10	22.57 ± 0.10	22.42 ± 0.10	22.04 ± 0.10	21.52 ± 0.10	21.35 ± 0.10	21.16 ± 0.10	20.92 ± 0.10	20.51 ± 0.10	20.77 ± 0.10	20.73 ± 0.10	21.14 ± 0.10	21.04 ± 0.10
66	150.175 61	2.401 59	26.00 ± 0.16	25.41 ± 0.10	25.08 ± 0.10	24.45 ± 0.10	24.13 ± 0.10	23.93 ± 0.17	22.92 ± 0.10	22.40 ± 0.10	21.68 ± 0.10	20.71 ± 0.10	20.43 ± 0.10	22.84 ± 0.10	22.30 ± 0.10
67	150.111 32	2.403 20	–	26.34 ± 0.23	26.22 ± 0.29	25.87 ± 0.28	26.72 ± 0.50	25.12 ± 0.51	24.68 ± 0.41	23.92 ± 0.32	23.31 ± 0.22	–	–	24.64 ± 0.20	23.94 ± 0.12
68	150.130 01	2.252 69	–	–	–	26.29 ± 0.41	26.44 ± 0.39	–	–	24.34 ± 0.47	23.04 ± 0.17	22.26 ± 0.10	21.78 ± 0.10	24.78 ± 0.23	24.04 ± 0.13
71	150.071 94	2.238 67	25.67 ± 0.12	24.99 ± 0.10	24.18 ± 0.10	23.16 ± 0.10	23.28 ± 0.10	22.56 ± 0.10	22.23 ± 0.10	21.88 ± 0.10	21.38 ± 0.10	21.12 ± 0.10	21.45 ± 0.10	22.20 ± 0.10	21.88 ± 0.10
72	150.064 56	2.329 03	23.81 ± 0.10	22.98 ± 0.10	22.28 ± 0.10	21.96 ± 0.10	21.66 ± 0.10	21.54 ± 0.10	21.56 ± 0.10	21.15 ± 0.10	20.66 ± 0.10	20.35 ± 0.10	20.00 ± 0.10	21.46 ± 0.10	21.23 ± 0.10
74	150.070 66	2.305 14	–	25.51 ± 0.11	24.75 ± 0.10	24.48 ± 0.10	24.49 ± 0.10	24.40 ± 0.26	24.03 ± 0.22	23.46 ± 0.21	22.99 ± 0.16	22.84 ± 0.10	22.40 ± 0.10	24.52 ± 0.18	23.62 ± 0.10
75	150.159 33	2.296 80	–	–	26.54 ± 0.39	25.83 ± 0.27	25.17 ± 0.12	24.71 ± 0.35	23.80 ± 0.18	22.82 ± 0.12	22.13 ± 0.10	21.24 ± 0.10	20.95 ± 0.10	23.40 ± 0.10	22.84 ± 0.10
77	150.070 27	2.422 97	23.42 ± 0.10	22.90 ± 0.10	22.40 ± 0.10	21.75 ± 0.10	21.66 ± 0.10	21.60 ± 0.10	21.44 ± 0.10	21.26 ± 0.10	20.98 ± 0.10	20.96 ± 0.10	21.39 ± 0.10	21.30 ± 0.10	21.17 ± 0.10
78	150.099 44	2.404 87	–	26.80 ± 0.34	25.83 ± 0.20	25.92 ± 0.29	25.47 ± 0.16	24.99 ± 0.45	24.50 ± 0.35	23.64 ± 0.25	23.14 ± 0.19	22.38 ± 0.10	21.88 ± 0.10	24.30 ± 0.15	23.77 ± 0.10
81	150.125 82	2.413 54	25.95 ± 0.16	23.98 ± 0.10	22.83 ± 0.10	21.50 ± 0.10	21.00 ± 0.10	20.76 ± 0.10	20.55 ± 0.10	20.50 ± 0.10	20.65 ± 0.10	21.50 ± 0.10	21.95 ± 0.10	20.53 ± 0.10	20.45 ± 0.10
84	150.111 54	2.409 57	23.05 ± 0.10	22.29 ± 0.10	21.57 ± 0.10	21.28 ± 0.10	21.10 ± 0.10	21.09 ± 0.10	20.91 ± 0.10	20.78 ± 0.10	20.57 ± 0.10	21.34 ± 0.10	21.46 ± 0.10	20.90 ± 0.10	20.73 ± 0.10
89	150.162 55	2.268 08	24.39 ± 0.10	24.16 ± 0.10	23.88 ± 0.10	23.14 ± 0.10	22.88 ± 0.10	22.81 ± 0.10	22.59 ± 0.10	22.50 ± 0.10	22.29 ± 0.10	22.27 ± 0.10	22.33 ± 0.10	22.54 ± 0.10	22.43 ± 0.10
91	150.070 60	2.289 20	–	–	–	26.52 ± 0.51	25.87 ± 0.23	–	24.91 ± 0.50	23.76 ± 0.28	22.53 ± 0.11	21.69 ± 0.10	21.30 ± 0.10	24.19 ± 0.14	23.58 ± 0.10
92	150.059 16	2.399 82	26.21 ± 0.20	25.31 ± 0.10	24.41 ± 0.10	23.67 ± 0.10	22.92 ± 0.10	22.59 ± 0.10	22.18 ± 0.10	21.49 ± 0.10	21.08 ± 0.10	20.32 ± 0.10	20.43 ± 0.10	21.97 ± 0.10	21.46 ± 0.10
93	150.057 85	2.427 23	25.93 ± 0.16	24.16 ± 0.10	22.58 ± 0.10	21.25 ± 0.10	20.73 ± 0.10	20.39 ± 0.10	19.91 ± 0.10	19.33 ± 0.10	18.84 ± 0.10	18.85 ± 0.10	19.34 ± 0.10	19.89 ± 0.10	19.38 ± 0.10
98	150.161 86	2.340 92	23.10 ± 0.10	22.38 ± 0.10	21.54 ± 0.10	20.61 ± 0.10	20.28 ± 0.10	20.03 ± 0.10	19.73 ± 0.10	19.34 ± 0.10	18.98 ± 0.10	19.11 ± 0.10	19.60 ± 0.10	19.73 ± 0.10	19.40 ± 0.10
103	150.085 14	2.381 95	–	26.55 ± 0.27	26.02 ± 0.24	26.25 ± 0.40	25.46 ± 0.16	–	–	24.03 ± 0.35	23.48 ± 0.26	23.02 ± 0.10	22.59 ± 0.10	24.92 ± 0.27	24.23 ± 0.15
105	150.164 26	2.408 81	–	25.57 ± 0.11	24.23 ± 0.10	23.13 ± 0.10	22.60 ± 0.10	22.27 ± 0.10	21.96 ± 0.10	21.57 ± 0.10	21.21 ± 0.10	20.92 ± 0.10	20.95 ± 0.10	21.91 ± 0.10	21.58 ± 0.10

Table A4. The optical–infrared photometry for the SCUBA-2 identifications which lie outside the CANDELS *HST* imaging. The table gives CFHTLS optical, Subaru z'-band, UltraVISTA near-infrared and IRAC mid-infrared AB magnitudes measured through 3 arcsec-diameter apertures. Errors are the 1σ values with a minimum adopted error of 0.1 mag.

ID	RA	DEC	u	g	r	i	z	Y	J	H	Ks	3.6 μm	4.5 μm	5.8 μm	8.0 μm
11	150.043 26	2.373 48	–	–	–	26.85 ± 0.48	25.86 ± 0.20	–	24.12 ± 0.22	23.29 ± 0.15	22.45 ± 0.10	21.30 ± 0.10	20.92 ± 0.10	20.72 ± 0.10	21.18 ± 0.11
17	150.207 97	2.383 08	27.27 ± 0.45	26.36 ± 0.16	26.11 ± 0.18	25.91 ± 0.18	25.91 ± 0.21	–	24.92 ± 0.52	24.31 ± 0.44	23.65 ± 0.26	22.66 ± 0.10	22.15 ± 0.10	21.65 ± 0.10	21.12 ± 0.11
25	150.037 29	2.340 57	–	27.76 ± 0.72	26.31 ± 0.22	25.73 ± 0.15	25.87 ± 0.20	–	25.08 ± 0.63	23.41 ± 0.17	23.10 ± 0.15	22.48 ± 0.10	22.10 ± 0.10	21.49 ± 0.10	22.08 ± 0.22
31	150.052 48	2.245 55	27.07 ± 0.36	25.62 ± 0.10	24.77 ± 0.10	24.27 ± 0.10	23.89 ± 0.10	23.54 ± 0.11	22.91 ± 0.10	21.85 ± 0.10	21.21 ± 0.10	20.61 ± 0.10	20.37 ± 0.10	20.21 ± 0.10	20.52 ± 0.10
33	150.040 98	2.280 63	–	–	–	–	–	–	–	–	–	22.83 ± 0.10	22.46 ± 0.10	21.97 ± 0.10	21.85 ± 0.20
42	150.027 54	2.345 77	25.86 ± 0.10	25.18 ± 0.10	24.28 ± 0.10	23.33 ± 0.10	22.84 ± 0.10	22.59 ± 0.10	22.05 ± 0.10	21.66 ± 0.10	21.16 ± 0.10	21.04 ± 0.10	21.36 ± 0.10	21.03 ± 0.10	21.79 ± 0.18
47	150.048 25	2.251 44	–	–	–	–	26.80 ± 0.54	–	–	23.78 ± 0.25	22.88 ± 0.12	21.81 ± 0.10	21.40 ± 0.10	20.72 ± 0.10	21.07 ± 0.10
48	150.021 41	2.288 67	–	26.31 ± 0.15	25.30 ± 0.10	24.87 ± 0.10	24.80 ± 0.10	24.73 ± 0.36	24.28 ± 0.26	23.22 ± 0.14	22.46 ± 0.10	21.81 ± 0.10	21.57 ± 0.10	21.27 ± 0.10	21.21 ± 0.11
51	150.036 52	2.286 17	26.01 ± 0.12	24.99 ± 0.10	24.59 ± 0.10	24.28 ± 0.10	23.97 ± 0.10	23.77 ± 0.14	23.04 ± 0.10	22.68 ± 0.10	21.90 ± 0.10	21.65 ± 0.10	21.49 ± 0.10	21.73 ± 0.10	22.50 ± 0.36
54	150.042 41	2.299 85	–	–	27.33 ± 0.68	–	26.42 ± 0.35	–	24.86 ± 0.49	23.72 ± 0.23	22.85 ± 0.12	22.12 ± 0.10	21.85 ± 0.10	21.78 ± 0.10	21.28 ± 0.13
56	150.050 02	2.386 07	–	27.23 ± 0.38	26.84 ± 0.38	26.38 ± 0.29	26.63 ± 0.44	–	–	24.52 ± 0.56	23.98 ± 0.37	23.11 ± 0.10	22.89 ± 0.10	–	–
73	150.209 62	2.355 25	23.48 ± 0.10	21.60 ± 0.10	20.41 ± 0.10	19.63 ± 0.10	19.24 ± 0.10	18.95 ± 0.10	18.43 ± 0.10	17.98 ± 0.10	17.65 ± 0.10	18.07 ± 0.10	18.24 ± 0.10	–	–
79	150.041 18	2.328 13	–	–	27.37 ± 0.71	26.42 ± 0.30	26.00 ± 0.23	–	24.38 ± 0.29	23.81 ± 0.26	22.59 ± 0.10	21.80 ± 0.10	21.55 ± 0.10	21.23 ± 0.10	21.89 ± 0.21
83	150.024 92	2.312 87	26.26 ± 0.16	25.74 ± 0.10	25.22 ± 0.10	24.59 ± 0.10	24.01 ± 0.10	23.48 ± 0.10	23.07 ± 0.10	22.37 ± 0.10	21.94 ± 0.10	21.55 ± 0.10	21.31 ± 0.10	21.58 ± 0.10	21.80 ± 0.18
86	150.051 66	2.305 85	25.09 ± 0.10	24.76 ± 0.10	24.35 ± 0.10	23.61 ± 0.10	23.03 ± 0.10	22.41 ± 0.10	21.80 ± 0.10	21.29 ± 0.10	20.86 ± 0.10	20.35 ± 0.10	20.22 ± 0.10	–	–
87	150.224 34	2.356 44	–	27.18 ± 0.36	26.52 ± 0.27	26.51 ± 0.33	26.37 ± 0.33	–	–	24.34 ± 0.45	23.62 ± 0.25	23.04 ± 0.10	22.73 ± 0.10	–	21.88 ± 0.23
88	150.054 56	2.275 35	26.77 ± 0.18	26.06 ± 0.10	25.52 ± 0.10	24.82 ± 0.10	24.02 ± 0.10	23.67 ± 0.10	22.87 ± 0.10	22.12 ± 0.10	21.26 ± 0.10	21.24 ± 0.10	20.85 ± 0.10	–	–
95	150.016 40	2.320 96	–	27.66 ± 0.63	26.83 ± 0.38	26.35 ± 0.28	25.89 ± 0.20	–	24.97 ± 0.55	23.50 ± 0.19	22.91 ± 0.12	22.41 ± 0.10	22.13 ± 0.10	21.79 ± 0.10	21.61 ± 0.16
99	150.210 20	2.311 67	24.05 ± 0.10	23.12 ± 0.10	22.14 ± 0.10	21.16 ± 0.10	20.88 ± 0.10	20.70 ± 0.10	20.34 ± 0.10	19.86 ± 0.10	19.37 ± 0.10	19.23 ± 0.10	19.59 ± 0.10	19.49 ± 0.10	19.51 ± 0.10
102	150.037 45	2.271 86	25.07 ± 0.10	24.42 ± 0.10	24.09 ± 0.10	23.66 ± 0.10	23.50 ± 0.10	22.97 ± 0.10	22.48 ± 0.10	22.08 ± 0.10	21.68 ± 0.10	21.07 ± 0.10	20.82 ± 0.10	20.81 ± 0.10	21.18 ± 0.11

Table A5. The derived physical properties of all 106 sources in the SCUBA-2 sample. The columns show, respectively, SCUBA-2 source number, optical spectroscopic redshift (should it exist for a robust ID), optical–infrared photometric redshift $z_{\rm p}$, the 'long-wavelength' photometric redshift $z_{\rm LW}$, the normalized redshift offset $r = (z_{\rm LW} - z_{\rm p})/(1 + z_{\rm p})$ (see Section 4.2), a flag indicating the status of the redshift information, and our final adopted redshift (with estimated errors), star formation rate (SFR) and stellar mass ($M_\star$). If a source's optical/near-infrared ID was rejected on the basis of an excessive value of r, it is flagged here with 0, if accepted it is flagged with 1 and if no ID was found the flag is set to 2. For objects flagged with 1 the final redshift z is the optical–infrared photometric redshift $z_{\rm p}$ (or $z_{\rm spec}$ if it exists), and therefore a stellar mass can be estimated for the galaxy and is given in the final column. If the flag is 0 or 2, the final adopted redshift z becomes $z_{\rm LW}$, but no stellar mass can be calculated due to the absence of any optical–infrared photometry. The last column gives the source for the spectroscopic redshifts. These include 11 redshifts from DR1 of the zCOSMOS redshift survey undertaken in the COSMOS field with the VIMOS spectrograph (Lilly et al. 2007), 2 redshifts obtained as a part of the 3D-HST observations of the COSMOS field (Brammer et al. 2012; Skelton et al. 2014) and 2 redshifts from the spectroscopic survey undertaken in the COSMOS field with DEIMOS spectrograph (PI: Jehan Kartheltepe).

ID SC850-	$z_{\rm spec}$	$z_{\rm p}$	$z_{\rm LW}$	r	flag	z	SFR ($\rm M_\odot\,yr^{-1}$)	$\log(M_\star)$ ($\rm M_\odot$)	Source
1	–	$1.35^{+0.10}_{-0.10}$	$3.30^{+0.22}_{-0.14}$	0.83	0	$3.30^{+0.22}_{-0.14}$	282.8 ± 32.8	–	–
2	0.3600	$0.39^{+0.11}_{-0.09}$	$3.05^{+0.19}_{-0.19}$	1.98	0	$3.05^{+0.19}_{-0.19}$	171.2 ± 11.2	–	VIMOS
3	–	–	$3.53^{+0.30}_{-0.30}$	–	2	$3.53^{+0.30}_{-0.30}$	447.6 ± 14.5	–	–
4	–	$1.51^{+0.19}_{-0.11}$	$2.09^{+0.08}_{-0.10}$	0.23	1	$1.51^{+0.19}_{-0.11}$	325.4 ± 9.6	$10.21^{+0.77}_{-0.45}$	–
5	–	$2.21^{+0.24}_{-0.21}$	$2.03^{+0.11}_{-0.10}$	−0.06	1	$2.21^{+0.24}_{-0.21}$	444.3 ± 13.1	$10.36^{+0.77}_{-0.68}$	–
6	–	$2.50^{+0.20}_{-0.15}$	$2.28^{+0.16}_{-0.11}$	−0.06	1	$2.50^{+0.20}_{-0.15}$	490.2 ± 15.1	$11.35^{+0.65}_{-0.49}$	–
7	–	$2.87^{+0.18}_{-0.17}$	$2.50^{+0.15}_{-0.16}$	−0.10	1	$2.87^{+0.18}_{-0.17}$	447.6 ± 14.5	$11.01^{+0.51}_{-0.48}$	–
8	–	$2.44^{+0.36}_{-0.24}$	$2.87^{+0.28}_{-0.28}$	0.12	1	$2.44^{+0.36}_{-0.24}$	356.2 ± 17.5	$9.54^{+1.00}_{-0.67}$	–
9	–	$1.75^{+0.15}_{-0.40}$	$2.20^{+0.20}_{-0.15}$	0.16	1	$1.75^{+0.15}_{-0.40}$	261.5 ± 13.3	$10.45^{+0.57}_{-1.52}$	–
10	–	$2.51^{+0.29}_{-0.26}$	$2.28^{+0.31}_{-0.22}$	−0.07	1	$2.51^{+0.29}_{-0.26}$	279.8 ± 14.2	$10.94^{+0.90}_{-0.81}$	–
11	–	$1.63^{+0.42}_{-0.13}$	$2.13^{+0.10}_{-0.11}$	0.19	1	$1.63^{+0.42}_{-0.13}$	261.1 ± 13.9	$10.82^{+1.73}_{-0.53}$	–
12	–	–	$3.47^{+0.65}_{-0.50}$	–	2	$3.47^{+0.65}_{-0.50}$	409.6 ± 17.8	–	–
13	–	$1.03^{+0.12}_{-0.13}$	$2.13^{+0.17}_{-0.16}$	0.54	0	$2.13^{+0.17}_{-0.16}$	261.5 ± 13.3	–	–
14	–	$2.18^{+0.17}_{-0.13}$	$1.44^{+0.05}_{-0.05}$	−0.23	1	$2.18^{+0.17}_{-0.13}$	409.6 ± 17.8	$11.04^{+0.59}_{-0.45}$	–
15	–	$2.30^{+0.20}_{-0.20}$	$2.64^{+0.41}_{-0.36}$	0.10	1	$2.30^{+0.20}_{-0.20}$	186.9 ± 11.1	$10.93^{+0.66}_{-0.66}$	–
16	0.6670	$0.99^{+0.11}_{-0.09}$	$1.77^{+0.08}_{-0.07}$	0.66	0	$1.77^{+0.08}_{-0.07}$	69.5 ± 5.0	$10.64^{+0.59}_{-0.48}$	VIMOS
17	–	$2.76^{+0.29}_{-0.51}$	$2.66^{+0.26}_{-0.17}$	−0.03	1	$2.76^{+0.29}_{-0.51}$	442.9 ± 25.7	$10.79^{+0.83}_{-1.46}$	–
18	–	$1.94^{+0.21}_{-0.19}$	$1.45^{+0.05}_{-0.03}$	−0.17	1	$1.94^{+0.21}_{-0.19}$	429.9 ± 16.2	$10.68^{+0.76}_{-0.69}$	–
19	–	$2.48^{+0.52}_{-1.18}$	$2.29^{+0.31}_{-0.22}$	−0.05	1	$2.48^{+0.52}_{-1.18}$	257.0 ± 15.5	$10.95^{+1.64}_{-3.71}$	–
20	–	$2.19^{+0.11}_{-0.09}$	$2.29^{+0.27}_{-0.17}$	0.03	1	$2.19^{+0.11}_{-0.09}$	255.5 ± 15.4	$11.17^{+0.39}_{-0.32}$	–
21	–	$1.98^{+0.42}_{-0.63}$	$1.70^{+0.13}_{-0.13}$	−0.09	1	$1.98^{+0.42}_{-0.63}$	203.6 ± 12.4	$10.89^{+1.53}_{-2.30}$	–
22	–	$1.51^{+0.94}_{-0.76}$	$2.17^{+0.35}_{-0.25}$	0.26	1	$1.51^{+0.94}_{-0.76}$	194.3 ± 13.5	$11.19^{+4.19}_{-3.39}$	–
23	–	$1.92^{+0.08}_{-0.17}$	$1.77^{+0.17}_{-0.13}$	−0.05	1	$1.92^{+0.08}_{-0.17}$	172.5 ± 11.1	$10.60^{+0.29}_{-0.62}$	–
24	–	$1.72^{+0.03}_{-0.12}$	$1.70^{+0.11}_{-0.13}$	−0.01	1	$1.72^{+0.03}_{-0.12}$	171.2 ± 11.2	$10.92^{+0.12}_{-0.48}$	–
25	–	$2.84^{+0.21}_{-0.24}$	$2.09^{+0.21}_{-0.22}$	−0.20	1	$2.84^{+0.21}_{-0.24}$	299.8 ± 21.2	$10.93^{+0.60}_{-0.68}$	–
26	2.6760	$2.61^{+0.09}_{-0.26}$	$1.44^{+0.10}_{-0.10}$	−0.34	1	2.68	217.9 ± 15.1	$10.48^{+0.26}_{-0.75}$	VIMOS
27	–	–	$2.49^{+0.44}_{-0.34}$	–	2	$2.49^{+0.44}_{-0.34}$	17.3 ± 2.0	–	–
28	–	$2.11^{+0.09}_{-0.16}$	$1.53^{+0.17}_{-0.11}$	−0.19	1	$2.11^{+0.09}_{-0.16}$	157.8 ± 10.7	$10.85^{+0.31}_{-0.56}$	–
29	0.7270	$0.71^{+0.14}_{-0.11}$	$2.41^{+0.24}_{-0.26}$	0.97	0	$2.41^{+0.24}_{-0.26}$	132.5 ± 19.5	–	VIMOS
30	–	–	$2.54^{+0.48}_{-0.41}$	–	2	$2.54^{+0.48}_{-0.41}$	128.9 ± 11.2	–	–
31	–	$2.47^{+0.08}_{-0.12}$	$2.29^{+0.22}_{-0.15}$	−0.05	1	$2.47^{+0.08}_{-0.12}$	450.5 ± 36.5	$11.23^{+0.26}_{-0.39}$	–
32	–	–	$2.92^{+0.64}_{-0.45}$	–	2	$2.92^{+0.64}_{-0.45}$	57.8 ± 7.9	–	–
33	–	$2.40^{+1.40}_{-0.65}$	$3.26^{+0.97}_{-0.56}$	0.25	1	$2.40^{+1.40}_{-0.65}$	206.6 ± 21.4	$11.66^{+4.80}_{-2.23}$	–
34	0.0010	$0.04^{+0.06}_{-0.04}$	$2.21^{+0.41}_{-0.21}$	2.21	0	$2.21^{+0.41}_{-0.21}$	164.2 ± 19.1	–	3D-HST
35	–	$1.36^{+0.24}_{-0.16}$	$2.06^{+0.23}_{-0.27}$	0.30	1	$1.36^{+0.24}_{-0.16}$	102.3 ± 10.5	$10.90^{+1.11}_{-0.74}$	–
36	–	$0.16^{+0.14}_{-0.11}$	$1.90^{+0.20}_{-0.14}$	1.50	0	$1.90^{+0.20}_{-0.14}$	132.5 ± 19.5	–	–
37	–	–	$1.56^{+0.20}_{-0.12}$	–	2	$1.56^{+0.20}_{-0.12}$	261.5 ± 13.3	–	–
38	–	$1.98^{+0.12}_{-0.28}$	$2.03^{+0.28}_{-0.39}$	0.02	1	$1.98^{+0.12}_{-0.28}$	174.5 ± 16.8	$10.71^{+0.43}_{-1.01}$	–
39	–	–	$2.58^{+0.63}_{-0.42}$	–	2	$2.58^{+0.63}_{-0.42}$	356.2 ± 17.5	–	–
40	–	$0.87^{+0.08}_{-0.17}$	$2.09^{+0.26}_{-0.32}$	0.65	0	$2.09^{+0.26}_{-0.32}$	447.6 ± 14.5	–	–
41	–	–	>3.92	–	2	>3.92	171.2 ± 11.2	–	–
42	0.9370	$0.96^{+0.09}_{-0.11}$	$2.20^{+0.36}_{-0.34}$	0.65	0	$2.20^{+0.36}_{-0.34}$	299.8 ± 21.2	–	DEIMOS

Table A5 – *continued*

ID SC850-	$z_{\rm spec}$	$z_{\rm p}$	$z_{\rm LW}$	r	flag	z	SFR ($M_\odot$ yr^{-1})	$\log(M_\star)$ ($M_\odot$)	
43	–	$1.86^{+0.44}_{-0.26}$	$2.83^{+0.79}_{-0.49}$	0.34	1	$1.86^{+0.44}_{-0.26}$	176.2 ± 22.1	$10.90^{+1.68}_{-0.99}$	–
44	0.1220	$0.13^{+0.12}_{-0.13}$	$1.96^{+0.58}_{-0.12}$	1.64	0	$1.96^{+0.58}_{-0.12}$	16.8 ± 2.9	–	VIMOS
45	–	$3.28^{+0.47}_{-0.13}$	$3.06^{+1.21}_{-0.70}$	−0.05	1	$3.28^{+0.47}_{-0.13}$	164.2 ± 19.1	$10.58^{+1.16}_{-0.32}$	–
46	–	–	$1.88^{+0.21}_{-0.14}$	–	2	$1.88^{+0.21}_{-0.14}$	132.5 ± 19.5	–	–
47	–	$2.55^{+0.75}_{-0.45}$	$2.63^{+0.63}_{-0.48}$	0.02	1	$2.55^{+0.75}_{-0.45}$	282.8 ± 32.8	$11.12^{+2.35}_{-1.41}$	–
48	–	$3.11^{+0.09}_{-0.16}$	$2.06^{+0.24}_{-0.25}$	−0.26	1	$3.11^{+0.09}_{-0.16}$	369.5 ± 37.6	$11.32^{+0.25}_{-0.44}$	–
49	–	$1.60^{+0.25}_{-0.20}$	$2.05^{+0.22}_{-0.30}$	0.17	1	$1.60^{+0.25}_{-0.20}$	108.5 ± 11.8	$9.48^{+0.91}_{-0.73}$	–
50	–	–	$1.95^{+0.87}_{-0.27}$	–	2	$1.95^{+0.87}_{-0.27}$	490.2 ± 15.1	–	–
51	–	$2.01^{+0.09}_{-0.11}$	$3.96^{+2.04}_{-1.12}$	0.65	1	$2.01^{+0.09}_{-0.11}$	152.4 ± 20.8	$10.82^{+0.32}_{-0.40}$	–
52	–	–	$3.18^{+2.82}_{-1.28}$	–	2	$3.18^{+2.82}_{-1.28}$	48.4 ± 8.2	–	–
53	–	$1.41^{+0.14}_{-0.11}$	$1.47^{+0.09}_{-0.08}$	0.02	1	$1.41^{+0.14}_{-0.11}$	120.6 ± 9.8	$11.51^{+0.67}_{-0.53}$	–
54	–	$3.09^{+0.26}_{-0.44}$	$2.09^{+0.34}_{-0.30}$	−0.24	1	$3.09^{+0.26}_{-0.44}$	204.5 ± 22.4	$11.02^{+0.70}_{-1.19}$	–
55	–	$1.74^{+0.11}_{-0.04}$	$1.25^{+0.13}_{-0.08}$	−0.18	1	$1.74^{+0.11}_{-0.04}$	128.9 ± 11.2	$11.27^{+0.45}_{-0.16}$	–
56	–	$2.80^{+0.35}_{-0.40}$	$2.13^{+0.48}_{-0.31}$	−0.18	1	$2.80^{+0.35}_{-0.40}$	194.9 ± 23.6	$10.76^{+0.99}_{-1.13}$	–
57	–	–	$3.36^{+2.47}_{-0.72}$	–	2	$3.36^{+2.47}_{-0.72}$	143.9 ± 17.0	–	–
58	–	–	$2.45^{+0.60}_{-0.49}$	–	2	$2.45^{+0.60}_{-0.49}$	157.8 ± 10.7	–	–
59	–	$1.69^{+0.11}_{-0.04}$	$2.04^{+0.22}_{-0.26}$	0.13	1	$1.69^{+0.11}_{-0.04}$	120.9 ± 13.8	$10.30^{+0.42}_{-0.15}$	–
60	–	–	>3.60	–	2	>3.60	25.6 ± 3.9	–	–
61	–	–	$1.47^{+0.16}_{-0.14}$	–	2	$1.47^{+0.16}_{-0.14}$	57.8 ± 7.9	–	–
62	–	$1.67^{+0.08}_{-0.17}$	$2.24^{+0.33}_{-0.26}$	0.21	1	$1.67^{+0.08}_{-0.17}$	129.6 ± 17.3	$10.96^{+0.33}_{-0.70}$	–
63	–	$0.81^{+0.29}_{-0.16}$	$5.41^{+0.59}_{-2.13}$	2.54	0	$5.41^{+0.59}_{-2.13}$	57.8 ± 7.9	–	–
64	–	$1.63^{+0.47}_{-0.28}$	$1.53^{+0.24}_{-0.15}$	−0.04	1	$1.63^{+0.47}_{-0.28}$	85.5 ± 9.4	$10.69^{+1.91}_{-1.14}$	–
65	2.4750	$0.13^{+0.07}_{-0.03}$	$2.09^{+0.33}_{-0.29}$	−0.11	1	2.48	132.5 ± 19.5	–	VIMOS
66	–	$1.77^{+0.08}_{-0.12}$	$1.57^{+0.27}_{-0.22}$	−0.07	1	$1.77^{+0.08}_{-0.12}$	143.9 ± 17.0	$10.84^{+0.31}_{-0.47}$	–
67	–	$2.34^{+0.11}_{-0.19}$	$1.96^{+0.50}_{-0.23}$	−0.11	1	$2.34^{+0.11}_{-0.19}$	134.3 ± 18.0	$10.09^{+0.33}_{-0.57}$	–
68	–	$0.78^{+0.22}_{-0.18}$	$1.60^{+0.23}_{-0.16}$	0.46	1	$0.78^{+0.22}_{-0.18}$	16.8 ± 2.9	$9.71^{+1.20}_{-0.98}$	–
69	–	–	>4.59	–	2	>4.59	129.6 ± 17.3	–	–
70	–	–	$4.97^{+1.03}_{-1.79}$	–	2	$4.97^{+1.03}_{-1.79}$	369.5 ± 37.6	–	–
71	–	$0.63^{+0.12}_{-0.03}$	$2.51^{+0.80}_{-0.44}$	1.15	0	$2.51^{+0.80}_{-0.44}$	450.5 ± 36.5	–	–
72	2.4460	$0.30^{+0.10}_{-0.05}$	$1.50^{+0.22}_{-0.15}$	−0.27	1	2.45	217.9 ± 15.1	–	VIMOS
73	0.1660	$0.18^{+0.07}_{-0.08}$	$0.42^{+0.02}_{-0.03}$	0.22	1	0.17	6.2 ± 0.0	$10.40^{+0.62}_{-0.71}$	VIMOS
74	–	$2.99^{+0.16}_{-0.09}$	$1.94^{+0.46}_{-0.31}$	−0.26	1	$2.99^{+0.16}_{-0.09}$	133.2 ± 19.2	$10.89^{+0.44}_{-0.25}$	–
75	–	$1.73^{+0.37}_{-0.13}$	$2.07^{+0.23}_{-0.31}$	0.12	1	$1.73^{+0.37}_{-0.13}$	109.6 ± 13.2	$10.62^{+1.44}_{-0.51}$	–
76	–	–	>3.58	–	2	>3.58	120.6 ± 9.8	–	–
77	–	$0.64^{+0.11}_{-0.09}$	$2.61^{+1.11}_{-0.65}$	1.20	0	$2.61^{+1.11}_{-0.65}$	57.8 ± 7.9	–	–
78	–	$2.21^{+0.19}_{-0.46}$	$2.61^{+1.09}_{-0.64}$	0.12	1	$2.21^{+0.19}_{-0.46}$	132.5 ± 19.5	$10.29^{+0.61}_{-1.47}$	–
79	–	$1.25^{+0.65}_{-0.35}$	$1.92^{+0.40}_{-0.24}$	0.30	1	$1.25^{+0.65}_{-0.35}$	48.4 ± 8.2	$9.63^{+2.78}_{-1.50}$	–
80	–	–	>3.42	–	2	>3.42	16.8 ± 2.9	–	–
81	–	$0.61^{+0.04}_{-0.11}$	>3.34	3.35	0	>3.34	134.3 ± 18.0	–	–
82	–	–	$2.63^{+1.38}_{-0.75}$	–	2	$2.63^{+1.38}_{-0.75}$	279.8 ± 14.2	–	–
83	–	$1.35^{+0.05}_{-0.15}$	$2.04^{+0.39}_{-0.30}$	0.29	1	$1.35^{+0.05}_{-0.15}$	70.5 ± 12.2	$10.31^{+0.22}_{-0.66}$	–
84	0.3500	$0.35^{+0.15}_{-0.10}$	>3.61	4.19	0	>3.61	134.3 ± 18.0	–	VIMOS
85	–	–	$1.51^{+0.26}_{-0.24}$	–	2	$1.51^{+0.26}_{-0.24}$	134.3 ± 18.0	–	–
86	1.4530	$1.36^{+0.19}_{-0.11}$	$1.38^{+0.22}_{-0.15}$	−0.03	1	1.45	75.8 ± 10.2	$11.11^{+0.89}_{-0.52}$	VIMOS
87	–	$2.94^{+0.31}_{-0.34}$	$4.82^{+1.18}_{-1.70}$	0.48	1	$2.94^{+0.31}_{-0.34}$	200.9 ± 35.4	$10.77^{+0.85}_{-0.93}$	–
88	–	$1.30^{+0.10}_{-0.10}$	$3.68^{+2.32}_{-1.28}$	1.03	0	$3.68^{+2.32}_{-1.28}$	206.6 ± 21.4	–	–
89	0.9050	$0.90^{+0.15}_{-0.10}$	$1.65^{+0.12}_{-0.20}$	0.39	1	0.91	25.6 ± 3.9	$9.78^{+0.77}_{-0.51}$	3D-HST
90	–	–	$1.96^{+1.14}_{-0.31}$	–	2	$1.96^{+1.14}_{-0.31}$	282.8 ± 32.8	–	–
91	–	$1.41^{+0.14}_{-0.21}$	$1.90^{+0.67}_{-0.36}$	0.20	1	$1.41^{+0.14}_{-0.21}$	64.6 ± 11.1	$10.53^{+0.61}_{-0.92}$	–
92	–	$1.12^{+0.03}_{-0.12}$	$1.37^{+0.18}_{-0.14}$	0.12	1	$1.12^{+0.03}_{-0.12}$	57.8 ± 7.9	$10.51^{+0.15}_{-0.59}$	–

Table A5 *– continued*

ID SC850-	$z_{\rm spec}$	$z_{\rm p}$	$z_{\rm LW}$	r	flag	z	SFR ($M_\odot$ yr^{-1})	$\log(M_\star)$ ($M_\odot$)	
93	0.6550	$0.64^{+0.06}_{-0.09}$	$3.41^{+1.67}_{-0.85}$	1.66	0	$3.41^{+1.67}_{-0.85}$	57.8 ± 7.9	–	DEIMOS
94	–	–	>4.31	–	2	>4.31	69.5 ± 5.0	–	–
95	–	$2.54^{+0.61}_{-0.29}$	$1.96^{+0.55}_{-0.24}$	− 0.16	1	$2.54^{+0.61}_{-0.29}$	192.0 ± 31.9	$10.67^{+1.84}_{-0.87}$	–
96	–	–	>3.12	–	2	>3.12	134.3 ± 18.0	–	–
97	–	–	>3.34	–	2	>3.34	171.2 ± 11.2	–	–
98	–	$0.69^{+0.16}_{-0.14}$	$1.13^{+0.09}_{-0.08}$	0.26	1	$0.69^{+0.16}_{-0.14}$	17.3 ± 2.0	$11.03^{+1.04}_{-0.91}$	–
99	–	$0.69^{+0.06}_{-0.09}$	$0.62^{+0.03}_{-0.04}$	− 0.07	1	0.75	91.0 ± 2.1	$10.54^{+0.37}_{-0.56}$	–
100	–	–	>3.53	–	2	>3.53	200.9 ± 35.4	–	–
101	–	–	>3.96	–	2	>3.96	16.8 ± 2.9	–	–
102	1.7410	$1.64^{+0.06}_{-0.14}$	$1.46^{+0.21}_{-0.16}$	− 0.10	1	1.74	133.5 ± 17.5	$10.40^{+0.24}_{-0.55}$	VIMOS
103	–	$2.95^{+0.20}_{-0.55}$	$1.68^{+0.22}_{-0.28}$	− 0.32	1	$2.95^{+0.20}_{-0.55}$	151.8 ± 21.6	$10.54^{+0.53}_{-1.47}$	–
104	–	–	$1.68^{+0.18}_{-0.29}$	–	2	$1.68^{+0.18}_{-0.29}$	134.3 ± 18.0	–	–
105	–	$0.67^{+0.08}_{-0.12}$	$2.09^{+0.72}_{-0.40}$	0.85	0	$2.09^{+0.72}_{-0.40}$	143.9 ± 17.0	–	–
106	–	–	$2.75^{+1.66}_{-0.83}$	–	2	$2.75^{+1.66}_{-0.83}$	6.2 ± 0.0	–	–

This paper has been typeset from a TEX/LATEX file prepared by the author.